Journal of Advanced Ceramics
先进陶瓷
ISSN 2226-4108
CN 10-1154/TQ
清华大学出版社 Tsinghua University Press
SciOpen

J Adv Ceram 2026, **15**: 9221383

https://doi.org/10.26599/JAC.2026.9221383

Research Article

Isotropic pressure-assisted defect regulation of PμSL-printed 5Y-ZrO_2 for high-reliability ultrathin dental veneers

Wenhua Tong[1,#], Yanru Shen[1,#], Pengjie Zhang[3,#], Chen Yang[4], Ying Jiang[4], Feng Wang[4], Suwei Dai[1], Shuyi Huang[1], Zhankun Pan[4], Jinhua Li[4], Weiwei Li[1], Yongsheng Zhou[2], Yuchun Sun[1], Lida Che[3,*], Xiang Wang[1,*]

[1] *Center of Digital Dentistry, Department of Prosthodontics, Peking University School and Hospital of Stomatology & National Center for Stomatology & National Clinical Research Center for Oral Diseases & National Engineering Research Center of Oral Biomaterials and Digital Medical Devices & Beijing Key Laboratory of Digital Stomatology & NHC Key Laboratory of Digital Stomatology & Key Laboratory of Digital Stomatology, Chinese Academy of Medical Sciences & NMPA Key Laboratory for Dental Materials, Center of Digital Dentistry, Department of Prosthodontics, Peking University School and Hospital of Stomatology & National Center for Stomatology & National Clinical Research Center for Oral Diseases & National Engineering Research Center of Oral Biomaterials and Digital Medical Devices & Beijing Key Laboratory of Digital Stomatology & NHC Key Laboratory of Digital Stomatology & Key Laboratory of Digital Stomatology, Chinese Academy of Medical Sciences & NMPA Key Laboratory for Dental Materials; Beijing 100081, China*

[2] *Department of Prosthodontics, Peking University School and Hospital of Stomatology, National Center for Stomatology, National Engineering Research Center of Oral Biomaterials and Digital Medical Devices, National Clinical Research Center for Oral Disease, Beijing Key Laboratory of Digital Stomatology, Research Center of Engineering and Technology for Computerized Dentistry Ministry of Health, 22 Zhongguancun Avenue South, Haidian District, Beijing 100081 China.*

[3] *CISRI HIPEX Technology Co., Ltd., Haidian, Beijing 100081, China*

[4] *BMF Nano Material Technology Co., Ltd; Shenzhen 518017, Guangdong Province, China*

[#] These authors contributed equally to this work.

* Corresponding authors.

Just Accepted

E-mail addresses: L. Che, chelida@hipex.cn;

X. Wang, xiangwang@pku.edu.cn

Received: July 6, 2026; Revised: September 12, 2026; Accepted: September 23, 2026

©The Author(s) 2026

Just Accepted

Abstract: Projection micro-stereolithography (PμSL) enables individualized zirconia ceramic restorations with complex freeform geometries and hundred-micrometre-scale thicknesses However, PμSL-printed ceramics often retain residual porosity, interlayer heterogeneity, and printing-induced defects after debinding, which limits full densification by conventional pressureless sintering. This limitation is particularly critical for ultrathin veneers because their reduced load-bearing thickness and intricate anatomical geometries increase sensitivity to residual pores, layer defects, and dimensional deviations. Although higher sintering temperatures can promote diffusion-driven densification, they also accelerate grain coarsening, which is detrimental to 5Y-ZrO_2 ceramics with limited transformation-toughening capability. Here, an isotropic pressure-assisted densification (iPAD) strategy was developed to regulate densification, defect chemistry, and microstructural uniformity in PμSL-printed 5Y-ZrO_2 ceramics. In this process, the PμSL-printed specimens were first pre-sintered and then further densified at elevated temperature under isotropic argon pressure to promote residual-pore closure and improve the overall properties of the ceramics. The optimized iPAD-treated ceramics achieved a relative density of 98.90%, together with a flexural strength of 951.30 ± 71.05 MPa, a Vickers hardness of 13.60 ± 0.07 GPa, a fracture toughness of 4.06 ± 0.30 MPa·$m^{1/2}$ and a transmittance of 56.15 ± 1.11% at 555 nm. XPS, EPR, TEM, and nanoindentation analyses reveal that the complete iPAD route results in a lower relative abundance of oxygen-vacancy-related defect states,

reduces defect-related scattering centers, and improves nanoscale mechanical uniformity. For ~80 μm zirconia veneers, iPAD increased the fracture load by approximately 35% while maintaining high manufacturing accuracy. This work provides a defect-regulated densification paradigm for high-reliability PμSL-printed 5Y-ZrO_2 ultrathin dental veneers.

Keywords: 5Y-ZrO_2 ceramics; projection micro-stereolithography; isotropic pressure-assisted densification; defect regulation; ultrathin dental veneers; mechanical and optical properties.

Just Accepted

1 Introduction

Yttria-stabilized zirconia ceramics are widely used in all-ceramic dental restorations because of their excellent biocompatibility, chemical stability, mechanical reliability, and teeth-like appearance [1-4]. Their phase constitution and performance strongly depend on yttria content. 5 mol% yttria-stabilized zirconia (5Y-ZrO_2) generally contains a relatively high fraction of optically isotropic cubic phase, which can reduce birefringence-related scattering and thereby favor translucency when other microstructural factors are comparable. However, the actual translucency of polycrystalline zirconia is also strongly governed by residual porosity, grain size and distribution, grain-boundary structure, surface roughness, and other scattering defects [5-8]. Accordingly, the successful clinical use of ultrathin 5Y-ZrO_2 veneers requires simultaneous control of phase constitution, microstructural defects, and surface quality.

At present, zirconia veneers are predominantly fabricated by subtractive CAD/CAM of partially sintered blanks followed by final densification [9,10]. However, milling can damage delicate margins; direct testing of Y-TZP blocks has shown incomplete marginal integrity and milling-related edge breakage on the order of 90-120 μm [11,12]. For laminate zirconia veneers, reducing the thickness from 0.5 to 0.3 mm significantly decreases fracture resistance [13], illustrating the structural challenge

of further thickness reduction by conventional CAD/CAM. More broadly, tool accessibility limits the reproduction of fine concave features, and the need to preserve adequate structural thickness can require additional tooth preparation to provide restorative space [14]. Projection micro-stereolithography (PμSL), a high-precision vat-photopolymerization technology, provides a promising route for directly fabricating individualized ceramic restorations with complex anatomical surfaces and hundred-micrometre-scale wall thicknesses [15-18]. Recent dental VPP studies have further shown that printing parameters affect dimensional accuracy [19], while layerwise photopolymerization can enable functionally graded restorations [20] and architecturally complex personalized dental devices [21].

However, the same photopolymerization process that enables this geometric freedom can also introduce forming inaccuracies. In particle-loaded ceramic slurries, light scattering and attenuation make the cure depth and lateral polymerization sensitive to slurry properties and exposure conditions [17,22-24], while inappropriate printing parameters can produce dimensional deviations [19]. In addition, ceramic green bodies produced by vat-photopolymerization contain high polymer loadings, and subsequent debinding can leave residual porosity, interlayer heterogeneity, weak layer interfaces, and other printing-related structural defects [22-24]. Pressureless sintering (PLS), which mainly relies on surface and grain-boundary diffusion, often cannot fully eliminate these internal defects [25,26]. Residual pores and interlayer flaws then act as crack-initiation sites and light-scattering centers, compromising both mechanical reliability and aesthetic performance. Together, these forming- and sintering-induced defects establish a direct link between the photopolymerization process and reduced translucency, dimensional accuracy, and structural reliability. This problem becomes more pronounced when printed zirconia is thinned to the hundred-micrometre scale. Because ultrathin veneers have a reduced load-bearing cross-section and shorter crack-propagation paths, a given pore, layer defect, oxygen-vacancy-related defect, or edge imperfection occupies a larger fraction of the structural volume and exerts a stronger influence on fracture initiation, light transmission, and marginal fidelity. Their

Just Accepted

complex freeform geometry further increases sensitivity to nonuniform shrinkage and local defect accumulation. Therefore, ultrathin PμSL-printed 5Y-ZrO_2 veneers impose stricter requirements on densification, defect tolerance, dimensional accuracy, and microstructural homogeneity than conventional bulk specimens or full crowns.

Increasing the sintering temperature is a straightforward way to accelerate diffusion and promote densification. However, this approach creates a densification-grain-growth dilemma for 5Y-ZrO_2 ceramics. Higher temperatures can reduce porosity but also promote grain coarsening or abnormal grain growth, which weakens strength and fracture resistance, especially in 5Y-ZrO_2 ceramics with limited transformation-toughening capability [27-30]. Thus, conventional pressureless sintering is poorly suited to simultaneously achieving high density, controlled microstructure, and reliable performance in ultrathin printed 5Y-ZrO_2 veneers. Several strategies have been explored to improve the densification and defect control of printed zirconia ceramics, including slurry optimization, sintering-condition optimization, two-step sintering, and other process-control approaches [29,31-34]. However, die-based field-assisted sintering is less compatible with individualized freeform restorations, while capsule-free HIP may still promote grain growth if the pre-sintering state and pressure-temperature schedule are not properly controlled [35,36]. A densification strategy that can close residual pores without sacrificing geometric complexity is therefore needed. Isotropic pressure-assisted densification (iPAD) is well matched to this requirement. Previous work indicates that HIP-based treatment can reduce process-related defects in zirconia while DLP can retain complex dental geometries [37-39]. These findings support iPAD as a promising route for closing residual pores while preserving the freeform geometry of ultrathin PμSL components. Because processing history may also affect oxygen-vacancy-related defect states [40-42], the complete iPAD route may additionally mitigate such defects. These considerations make iPAD particularly attractive for defect-sensitive PμSL-printed 5Y-ZrO_2 restorations.

Just Accepted

In this study, we developed a PμSL-pre-sintering-iPAD strategy for 5Y-ZrO_2 ultrathin ceramic veneers. In this context, iPAD denotes an application-specific, capsule-free HIP treatment in which pre-sintered PμSL components are exposed to elevated temperature and isotropic Ar pressure. The effects of this route on shrinkage behavior, dimensional accuracy, microstructure, phase composition, densification, mechanical properties, optical behavior, oxygen-vacancy-related defect states, and nanoscale mechanical uniformity were systematically investigated. Finally, zirconia veneers with a target thickness of ~80 μm, which was selected to explore the feasibility of fully additive no-preparation restorations, were fabricated to validate the practical applicability of this route. This work provides a systematic evaluation of the PμSL-pre-sintering-iPAD route for producing high-performance ultrathin 5Y-ZrO_2 dental veneers.

2 Materials and methods

2.1 Preparation and densification of PμSL-printed 5Y-ZrO_2 ceramics

A commercial 5Y-ZrO_2 slurry (BMF-PZSAMV-1, ~80 wt% solid loading, BMF Precision Tech Co., Ltd.) was used in this study. The corresponding 5Y-ZrO_2 powder (G5Y-020OQA) was purchased from Shandong Sinocera Functional Materials Co., Ltd. Its chemical composition is presented in Table S1.

Green bodies, including bar specimens (20 × 4 × 1.2 mm) and dental veneer structures with a designed thickness of 80 μm, were fabricated by stereolithography using a PμSL printer (microArch, BMF Precision Tech Inc., China) with a resolution of 10 μm. After printing, the samples were cleaned, air-dried, and debinded at 1000 ºC for 2 h in air using a debinding furnace (FMJ-07/11, Hefei Fischero Intelligent Equipment Co., Ltd). The debound specimens were divided into two groups for final densification: For pressureless sintering (PLS), specimens were sintered at 1450 - 1600 ºC for 2 h in air and are denoted as PLS-temperature, for example, PLS-1450 ºC. For isostatic pressure-assisted densification (iPAD), specimens were first pre-sintered at 1350 - 1450 ºC for 2 h in air, followed by high-pressure treatment at 1350 - 1450 ºC under 180 MPa in an argon atmosphere (HIPEX80, CISRI HIPEX Technology CO., China), with a heating rate 5 ºC·min^{-1} and a holding time of 2 h. After iPAD,

Just Accepted

all iPAD specimens were subjected to post-iPAD air annealing at 1000 ºC for 2 h. This treatment was intended to oxidatively remove possible carbonaceous residues introduced during the high-pressure treatment and to promote reoxidation and recovery of the oxygen stoichiometry of zirconia following exposure to the Ar atmosphere. The PLS specimens were not subjected to this additional annealing step because their final densification was conducted entirely in air and therefore did not expose them to the potentially reducing and carbon-contaminating environment associated with the high-pressure Ar treatment. Accordingly, comparisons between the PLS and iPAD specimens represent the effects of the complete processing routes rather than the isolated effect of pressure. The detailed temperature profiles for all debinding, pre-sintering, pressureless sintering, iPAD treatment, and decarbonization processes used in this study are presented in Fig. S1 of the Supplementary Information. The obtained ceramics are denoted as iPAD-sintering temperature, for example, iPAD-1350 ºC.

2.2 Characterization

The bulk chemical composition of the zirconia powder was determined by X-ray fluorescence spectroscopy (XRF, Rigaku, ZSX Primus III+, Japan). The specific surface area of the powder was measured using a fully automated surface area and porosity analyzer (TriStar II Plus 3030, Micromeritics, USA) based on the Brunauer-Emmett-Teller (BET) method. The powder morphology shown in Fig. 1(b) was observed using scanning electron microscopy (SEM; ZEISS Sigma 360, Germany). The particle size analysis was performed using Nano Measure software based on multiple randomly selected SEM fields, with the projected dimensions of the powder particles being measured. Since mild agglomeration is an inherent feature of the powder and contributes to its apparent particle size distribution, mildly agglomerated particles with identifiable outlines were included in the analysis. Only severely overlapping regions for which the external boundaries could not be reliably determined were excluded. At least 200 individual powder particles or distinguishable small agglomerates were measured, from which the mean particle size and particle size frequency distribution were calculated.

Just Accepted

The apparent density, bulk density, and apparent porosity of the ceramic samples were determined according to GB/T 25995-2010 (modified adoption of ISO 18754:2003) using ultrapure water as the immersion medium (Archimedes method) [43]. The samples were dried at 100 ± 5 ℃ to a constant mass and weighed using an analytical balance (Mettler Toledo, ME204E/02, Switzerland) to obtain the dry mass (m_1, g). They were then completely immersed in water, boiled for at least 30 min, and cooled to room temperature in water. The buoyant mass of the saturated specimen (m_2, g) was measured using a suspension assembly after correcting for the mass of the empty basket. After removing the surface liquid with a damp absorbent cloth, the saturated mass in air (m_3, g) was immediately measured. The apparent density (ρ_a, g cm^{-3}), bulk density (ρ_b, g cm^{-3}), and apparent porosity (π_a, %) were calculated as follows:

$$\rho_a = \frac{m_1}{m_1 - m_2} \times \rho_1 \quad (1)$$

$$\rho_b = \frac{m_1}{m_3 - m_2} \times \rho_1 \quad (2)$$

$$\pi_a = \frac{m_3 - m_1}{m_3 - m_2} \times 100 \quad (3)$$

where ρ_1 is the density of ultrapure water at the test temperature.

The phase compositions of the samples were analyzed using an X-ray diffractometer (XRD, Bruker D8 Advance, Germany). The measurements were performed using Ni-filtered Cu Kα radiation (λ = 1.54059 Å) and a silicon-based position-sensitive one-dimensional detector at a tube voltage of 40 kV and a tube current of 40 mA. The diffraction patterns were collected over a 2θ range of 10°-90° with a step size of 0.01° and a counting time of 0.4 s per step, corresponding to a nominal acquisition time of approximately 53.3 min for each sample. Rietveld full-pattern refinement was performed using GSAS-II to determine the crystalline phase fractions of the samples. The refinement quality was evaluated using the profile residual (R_p), weighted-profile residual (R_{wp}), and χ^2, together with inspection of the observed-calculated difference profiles. Because these indicators depend on counting statistics, background level, instrumental resolution, and model complexity, no universal numerical cutoff alone defines a satisfactory Rietveld refinement; χ^2 should ideally approach 1 but may exceed 1

Just Accepted

when systematic deviations are greater than the counting-statistical uncertainties [44,45]. After polishing and thermal etching at 100 °C below the final sintering temperature for 5 min, surface and fracture morphologies were observed by scanning electron microscopy (SEM, ZEISS Sigma 360, Germany) [43]. Grain sizes were statistically analyzed from SEM images by the line-intercept method with Nano Measure software, based on at least 200 grains. Surface morphologies of the polished and etched samples were further examined by atomic force microscopy (AFM, ICSPI Redux, Canada). Grain-boundary groove widths were statistically estimated from AFM height profiles using the full width at half maximum (FWHM) criterion in Gwyddion software, based on at least 100 measurements [46,47].

Thin lamellae were prepared by focused ion beam milling (FIB, Helios 5 Hydra CX, USA), followed by microstructural observation and elemental mapping using transmission electron microscopy (TEM, FEI Talos F200X, USA). Spatial distributions of hardness and elastic modulus were measured using a nanoindenter (Bruker Hysitron Nanoindenter TI-990, Germany). To minimize the effects of adsorption, contamination, and chemical alterations associated with the original external surfaces, freshly fractured surfaces exposing the specimen interior were analyzed by X-ray photoelectron spectroscopy (XPS, Thermo Scientific K-Alpha, USA) to characterize their chemical states. Oxygen-vacancies related signals were characterized by electron paramagnetic resonance spectroscopy (EPR, Bruker EMXplus-6/1, Germany). Surface roughness of zirconia thin plates was measured using a three-dimensional optical profilometer (S neox A90, Sensofar, Spain). The final-sintered veneer specimens were scanned using a high-precision industrial scanner (ATOS Q, GOM, Germany). The scanned datasets were imported into the corresponding analysis software (Inspect 2018, GOM, Germany) and compared with the CAD model. Pre-alignment followed by best-fit registration was performed using the iterative closest point (ICP) algorithm, and deviation color maps were generated.

2.3 Mechanical property measurements

Just Accepted

In accordance with GB/T 6569-2006, the three-point flexural strength was measured using a universal testing machine (INSTRON 34TM-10, USA) at a loading rate of 0.5 mm·s^{-1} and a support span of 12 mm. The specimens were ground and polished into rectangular bars with dimensions of 19 × 3.8 × 1 mm using a grinding and polishing machine (ALLIED, M-PREP 5, USA). At least three specimens were tested for each group. Flexural strength was calculated using Eq. (4):

$$\sigma_f = \frac{3Pl}{2bh^2} \quad (4)$$

where σ_f is the flexural strength (MPa), P is the fracture load (N), l is the support span (mm), and b and h are the specimen width and thickness (mm), respectively.

Hardness and fracture toughness were determined by the indentation fracture method (ISO 14705: 2016) using a Vickers hardness tester (MATSUZAWA, Via-S, Japan). Mirror-polished specimens were prepared using an automatic precision polishing system (LEICA, EM TXP, Germany). Indentation marks were produced using a diamond indenter under a load of 19.6 N for 10 s. The crack radius (c, μm) and half-length of the indentation diagonal (a, μm) were observed and measured using a digital microscope. Fracture toughness, K_{Ic} (MPa·m$^{1/2}$), was evaluated based on the fundamental principles of ISO 21618:2025 and calculated using Eq. (5), as reported by Lankford [48,49]:

$$\left(\frac{K_{Ic}\Phi}{H\mathrm{a}^{1/2}}\right)\left(\frac{H}{E\Phi}\right)^{0.4} = 0.142\left(\frac{\mathrm{c}}{\mathrm{a}}\right)^{-1.56} \quad (5)$$

where H is the Vickers hardness (GPa), E is the Young's modulus (GPa), and Φ is the constraint factor. In this study, Φ was taken as 3, and E was assumed to be 220 GPa [50].

Based on previous studies and considering clinical operation procedures, a resin 3D printer (DLP1080E, Han's Laser, China) was used to fabricate molds for the veneer loading test [12,33]. A silicone rubber material (Meijiayin Type 3 Light Body, Huge Dental, China) was used as the load-transmitting medium. Compression tests were performed using a universal testing machine to simulate the clinical procedure of finger pressing during veneer placement. The load at fracture was recorded as the ultimate load (N) and used to evaluate the fracture resistance of the veneers.

Just Accepted

2.4 Optical property measurements

The optical properties of the samples were evaluated using a UV-vis-NIR spectrophotometer equipped with a 100 mm integrating sphere (Lambda 750 S, PerkinElmer, USA). The instrumental colour-measurement and reporting procedures were established with reference to ISO/TR 28642:2016. Because no international standard specifically addresses the total spectral transmittance of ultrathin, translucent bulk dental zirconia, the integrating-sphere measurement configuration was fully specified to ensure experimental reproducibility. Total transmittance (T, %) and contrast ratio (CR) were measured in the visible wavelength range of 380-780 nm to characterize ceramic translucency. The parameters were calculated according to the following Eqs. (6)-(7):

$$T=(I_t/I_0)\times 100\% \quad (6)$$

$$CR=Y_b/Y_w \quad (7)$$

where I_t is the transmitted light flux through the sample (mW cm^{-2}), including both direct and diffuse transmission, and I_0 is the incident light flux (mW cm^{-2}). Y_b represents the reflectance of the sample against a black background (%), whereas Y_w represents the reflectance against a white background (%). The contrast ratio ranges from 0.0 (completely transparent) to 1.0 (completely opaque,).

Ten specimens were prepared for each group. All specimens used for optical characterization were tested without surface polishing. Before measurement, the specimens were ultrasonically cleaned in ethanol and gently dried with compressed air to accelerate ethanol evaporation. According to the International Commission on Illumination (CIE S 017), the human eye exhibits the highest relative sensitivity to light at a wavelength of 555 nm under equal-energy conditions. Therefore, the value measured at 555 nm was selected for statistical analysis [51].

3 Results

3.1 Phase composition and microstructure of the powder

Fig. 1a shows the XRD pattern of the commercial 5Y-ZrO_2 powder. The powder is predominantly composed of cubic zirconia (*c*-ZrO_2, PDF#49-1642). The SEM image (Fig. 1b) and HRTEM image

Just Accepted

(Fig. 1c, d) reveal that the 5Y-ZrO_2 powder particles exhibit a quasi-spherical morphology with a certain degree of agglomeration. The particle size distribution (insert in Fig. 1b) is mainly concentrated in the range of 100-200 nm, with an average particle size of 170.65 nm. As shown in Fig. 1d, the lattice spacing of d = 0.296 nm corresponds to the (111) crystal plane of *c*-ZrO_2 (PDF#49-1642), consistent with the XRD analysis. BET specific surface area of the powder was measured to be 9.00 $m^2 \cdot g^{-1}$.

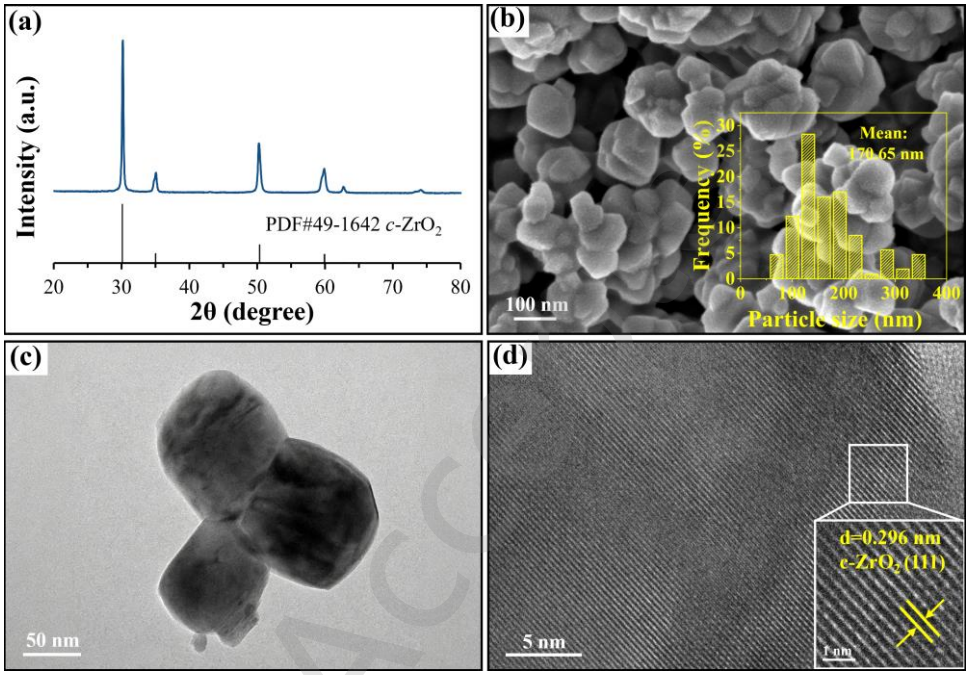


Fig. 1. Characterization of 5Y-ZrO_2 powder. (a) XRD pattern; (b) SEM image with particle size distribution inset; (c) TEM image; (d) HRTEM image showing the *c*-ZrO_2 (111) lattice fringes.

3.2 Exploration of pre-sintering conditions

Before iPAD treatment, ceramics are typically pre-sintered in air to close surface-connected pores, thereby preventing high-pressure gas infiltration and grain boundary cracking caused by trapped residual gases during subsequent densification [37,52]. Fig. 2 shows the thermally etched surfaces (Fig. 2a-c) and fracture cross-sections (Fig. 2d-f) of ceramics pre-sintered in air at 1350 °C, 1400 °C, and 1450 °C for 2 h, with the corresponding grain size distributions shown as insets in the fracture cross-sectional images. With increasing pre-sintering temperature, the grain size gradually increased. At 1350 °C and 1400 °C, a relatively loose internal microstructure was observed, and unclosed pores remained on the surface (circles in Fig. 2a, b), indicating that diffusion was insufficient to complete

pore closure at these lower temperatures. At low sintering temperatures, pore closure relies mainly on sluggish surface and grain-boundary diffusion, leaving residual open pores in the material [25,26]. When the pre-sintering temperature reached 1450 ºC, most of the surface pores were closed and densification was significantly improved. Some grains became relatively large (circled regions), which may be associated with enhanced grain growth at elevated temperatures. This phenomenon suggests that grain growth is initially constrained by pores, whereas pore closure facilitates freer grain growth, thereby increasing grain improving overall microstructural integrity [27,29]. Therefore, 1450 ºC was selected as the pre-sintering temperature for subsequent iPAD treatment because it provided the best balance among surface-connected pore closure, densification, and grain-growth control within the investigated temperature range.

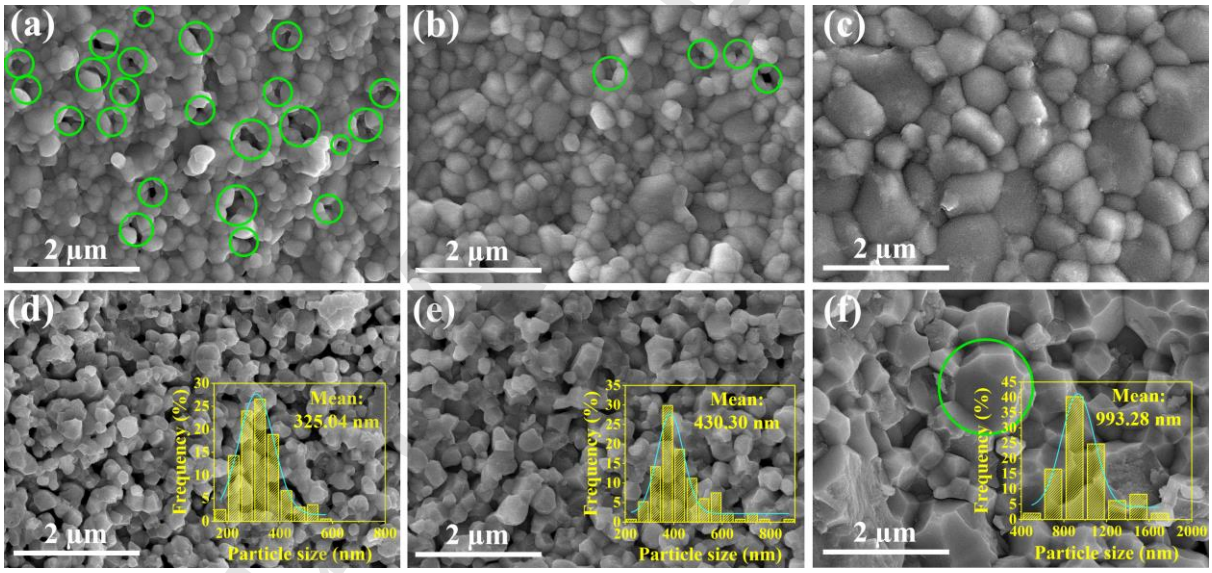


Fig. 2 Surface and fracture cross-sectional microstructures of ceramics pre-sintered at 1350 ºC (a, d), 1400 ºC (b, e), and 1450 ºC (c, f) for 2 h; the corresponding grain size distributions are shown as insets in the fracture cross-sectional images.

3.3 Shrinkage and densification behavior

After debinding at 1000 ºC, the PμSL green bodies showed only limited dimensional contraction, with a representative volume shrinkage of approximately 4.70%, indicating that binder removal and initial particle rearrangement were not sufficient to drive substantial densification. Representative final

treatments produced much larger shrinkage. The PLS-1500 ºC sample reached a volume shrinkage of approximately 49.50%, whereas the 1450 ºC pre-sintered ceramic showed a slightly lower value of approximately 48.35%, consistent with the role of pre-sintering in closing surface-connected pores rather than achieving full densification. After iPAD treatment, the volume shrinkage increased to approximately 50.88% at 1350 ºC and 50.91% at 1450 ºC, indicating that isotropic pressure promoted additional dimensional contraction under a reduced thermal budget. These representative shrinkage values are consistent with the SEM observations described below: pressureless sintering at 1500 ºC still left residual pores and local defects, whereas iPAD at 1450 ºC produced a denser and more homogeneous microstructure. Therefore, the shrinkage results support the interpretation that iPAD promotes residual pore closure and particle rearrangement beyond diffusion-driven PLS. Fig. 3 compares the surface morphologies and fracture cross-sectional morphologies of the PLS-1500 ºC and iPAD-1450 ºC ceramics. The PLS-1500 ºC sample still contained numerous irregular pores and local defects on the surface. Dispersed pores can be observed in the low-magnification SEM image (Fig. 3a), indicating that although pressureless sintering can promote overall densification, it is still difficult to eliminate the residual pore defects inherited from the printed green body. The high-magnification SEM image (Fig. 3b) and the grain-size distribution plot (inset in Fig. 3b) further show that the PLS-1500 ºC sample exhibited a broad grain-size distribution, with locally abnormally grown grains coexisting with fine grains, suggesting limited microstructural uniformity. Obvious intergranular pores, grain-boundary voids, and locally loose regions can still be observed in the fracture cross-sections (Fig. 3c, d). These defects weaken the bonding strength between grains and may act as preferential sites for crack initiation and propagation under external loading [30,53]. In contrast, the iPAD-1450 ºC sample exhibited a denser and more homogeneous microstructure. The number of surface pores was markedly reduced, and the overall surface became smoother and denser (Fig. 3e). In the high-magnification SEM image (Fig. 3f), clearly defined grain outlines and more tightly packed grains can be observed, without obvious large residual pores. The fracture cross-sectional morphologies (Fig. 3g, h) show that the

Just Accepted

interior of the iPAD sample consisted of closely packed grains, with significantly reduced intergranular pores and grain-boundary voids. Compared with the PLS sample, the iPAD sample showed a narrower grain-size distribution (inset in Fig. 3f), indicating that the synergistic effect of isotropic gas pressure and high-temperature diffusion during hot isostatic pressing effectively promoted residual pore closure, particle rearrangement, and grain-boundary bonding, thereby improving the overall densification and microstructural uniformity of the ceramics [37-39,54].

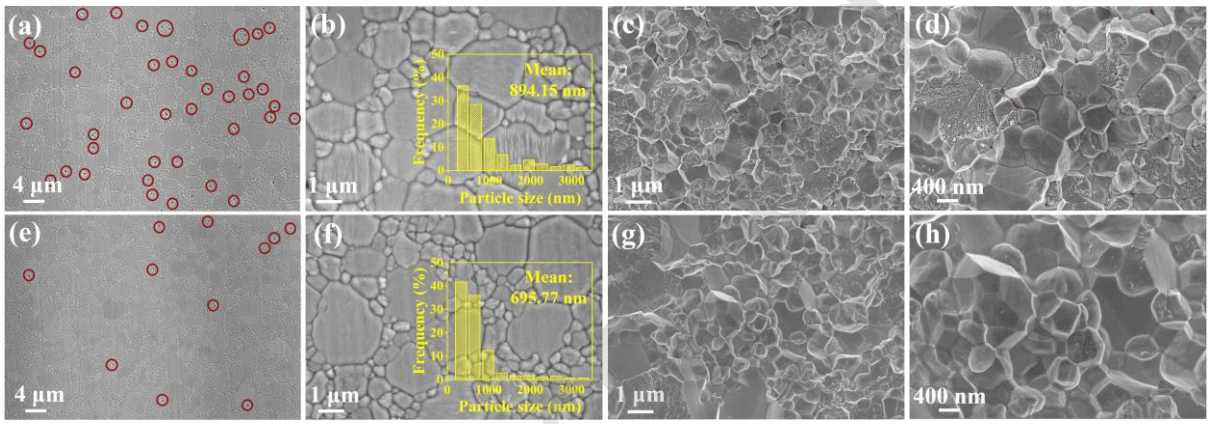


Fig. 3 Surface morphologies (a, b) and fracture cross-sectional morphologies (c, d) of ceramics after PLS sintering at 1500 ºC; surface morphologies (e, f) and fracture cross-sectional morphologies (g, h) of ceramics after iPAD sintering at 1450 ºC.

Fig. 4 further characterizes the three-dimensional surface morphologies, grain-boundary groove features, and apparent relative grain-boundary-to-surface energy ratios of the polished and thermally etched PLS-1500 ºC and iPAD-1450 ºC ceramics by AFM. The AFM image of the PLS-1500 ºC sample shows pronounced surface undulations and deep grain-boundary grooves (Fig. 4a). The height profiles extracted from the centers of the grain-boundary grooves (Fig. 4b) reveal that the grain-boundary regions of the PLS-1500 ºC sample are relatively wide and exhibit obvious morphological fluctuations. Based on the AFM height profiles, the average grain-boundary groove width statistically determined using the full width at half maximum (FWHM) method was 287.5 nm (Fig. 4c), indicating that the grain-boundary regions of the pressureless-sintered sample were relatively rough and that pronounced grain-boundary grooves had developed. These wide and deep grain-boundary grooves

Just Accepted

may be associated with insufficient residual pore elimination, nonuniform grain-boundary migration, and local grain coarsening during PLS [55,56]. In contrast, the iPAD-1450 ºC sample exhibited a smoother surface morphology (Fig. 4d) and clearer, narrower grain-boundary profiles (Fig. 4e). Its average grain-boundary groove width decreased to 127.6 nm (Fig. 4f), which was markedly smaller than that of the PLS-1500 ºC sample. This indicates that iPAD treatment effectively reduced the surface height fluctuations at grain boundaries and improved the morphological uniformity of the grain-boundary regions. This result is consistent with the high density, low porosity, and homogeneous fracture morphology observed by SEM, suggesting that the synergistic effect of isotropic pressure and high-temperature diffusion promoted residual pore closure, grain-boundary bonding, and microstructural homogenization.

To further compare the interfacial states produced by the different sintering routes, the apparent relative grain-boundary-to-surface energy ratio was estimated from the geometry of the grain-boundary grooves formed after thermal etching. During thermal etching, stable grain-boundary grooves form at the intersections between grain boundaries and free surfaces, and their equilibrium morphology is determined by the mechanical balance between the grain-boundary energy, γ_{gb}, and the surface energy, γ_s. The grain-boundary groove morphology of the thermally etched surface was measured by AFM, and the apparent γ_{gb}/γ_s ratio was estimated from the groove-root dihedral angle in the cross-sectional profile to compare the interfacial states produced by the different sintering routes. The basic relationship can be expressed as:

$$\frac{\gamma_{gb}}{\gamma_s} = 2\cos(\frac{\psi}{2}) \qquad (8)$$

where γ_{gb} is the grain-boundary energy (J m^{-2}), γ_s is the surface energy (J m^{-2}), and ψ is the dihedral angle formed by the tangents to the two free surfaces on both sides of the grain-boundary groove (º). Under the assumption of local capillary equilibrium, Eq. (8) describes the interfacial-energy balance at a thermally etched grain-boundary groove. Because the absolute grain-boundary and surface energies were not independently measured, γ_{gb}/γ_s is reported here as an apparent grain-boundary-to-

Just Accepted

surface energy ratio and is used only to compare specimens thermally etched and characterized under identical conditions. Similar dihedral-angle-based methods have been used to estimate apparent relative interfacial-energy ratios and examine their associations with grain-boundary structure and microstructural evolution [46,57].

As shown in Fig. 4h, the apparent γ_{gb}/γ_s ratio was 0.32 ± 0.08 for the PLS-1500 ºC sample and 0.51 ± 0.14 for the iPAD-1450 ºC sample. Combined with the AFM results, the PLS sample exhibited a lower relative grain-boundary energy but wider and deeper grain-boundary grooves, with pronounced morphological fluctuations in the grain-boundary regions. This suggests the possible presence of more residual defects, pores, or discontinuous bonding regions at the grain boundaries. In contrast, the iPAD sample showed a higher relative grain-boundary energy together with markedly narrower grain-boundary grooves and clearer, smoother grain-boundary profiles, indicating that iPAD promoted atomic diffusion, residual pore closure, and tighter intergranular bonding at the grain boundaries, thereby improving the continuity and stability of the grain-boundary structure.

It should be noted that a higher apparent relative grain-boundary energy ratio should not be interpreted in isolation as indicating a less stable or more defective grain boundary. The two AFM-derived parameters characterize different aspects of the thermally grooved interfaces. The apparent γ_{gb}/γ_s ratio, estimated from the groove-root dihedral angle under the local capillary-balance approximation, primarily describes the local balance between grain-boundary and surface energies. In contrast, the groove width and depth reflect the kinetic evolution of the thermally generated groove and can be affected by the etching temperature and duration, surface diffusivity, crystallographic orientation, interfacial anisotropy, and local surface geometry [46,58,59]. Therefore, the higher apparent γ_{gb}/γ_s ratio and the narrower grain-boundary grooves observed for the iPAD sample are not logically contradictory. Moreover, Eq. (8) provides a normalized grain-boundary-to-surface energy ratio rather than an absolute grain-boundary energy; consequently, changes in this ratio may originate from changes in γ_{gb}/γ_s, or both. For the 5Y-ZrO_2 ceramics investigated here, the higher apparent energy

Just Accepted

ratio of the iPAD sample occurred concurrently with narrower grooves, smaller surface-height fluctuations, higher density, lower porosity, and a more homogeneous microstructure. These observations indicate that iPAD simultaneously modified the local capillary geometry of the thermally grooved interfaces and improved the morphological uniformity of the grain-boundary regions. Accordingly, the apparent γ_{gb}/γ_s ratio is used here as a comparative descriptor of the thermally grooved interfacial state rather than as a direct measure of grain-boundary defect density, bonding strength, or stability.

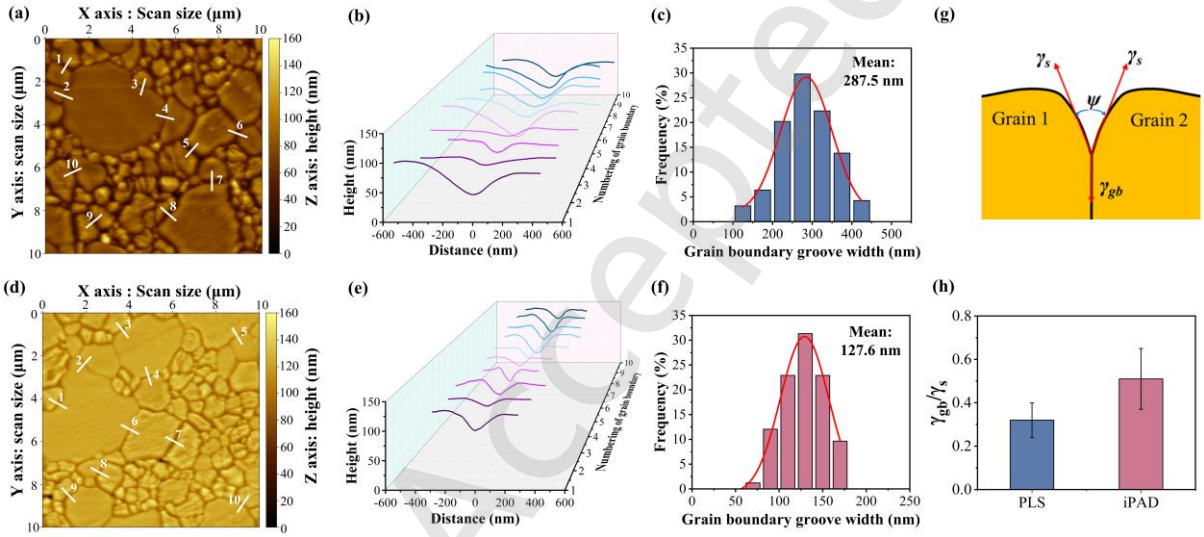


Fig. 4 AFM image of the ceramic surface after PLS sintering at 1500 °C (a), height profile across the center of the grain-boundary groove (b), and statistical distribution of grain-boundary groove width (c); AFM image of the ceramic surface after iPAD sintering at 1450 °C (d), height profile across the center of the grain-boundary groove (e), and statistical distribution of grain-boundary groove width (f); schematic illustration of the grain-boundary groove cross-section (g); apparent relative grain-boundary-to-surface energy ratios of the ceramic surfaces obtained under different sintering conditions (h). The 10 cross-sectional diagrams of the grain boundary grooves shown in (b) and (e) were respectively taken from the representative grain boundaries marked as 1 to 10 in (a) and (d).

3.4 Phase composition and densification of the ceramics

Fig. 5 shows the XRD patterns of the 5Y-ZrO_2 ceramics sintered under different conditions. As shown in Fig. 5a, all samples were mainly composed of tetragonal zirconia (*t*-ZrO_2, PDF#50-1089) and cubic

Just Accepted

zirconia (*c*-ZrO_2, PDF#49-1642), with no obvious monoclinic phase or other impurity phases detected. This indicates that the 5Y-ZrO_2 ceramics maintained a relatively stable *t*/*c* dual-phase structure after pressureless sintering at 1450-1600 °C and iPAD treatment at 1350 - 1450 °C. Further examination of the enlarged 2θ range of 33° - 36° (Fig. 5b) shows that the characteristic peaks of *t*-ZrO_2 and *c*-ZrO_2 can be more clearly distinguished in this region. All samples exhibited overlapping and splitting features of the *t*- and *c*-phase diffraction peaks within this angular range, further confirming the coexistence of tetragonal and cubic phases in the sintered ceramics.

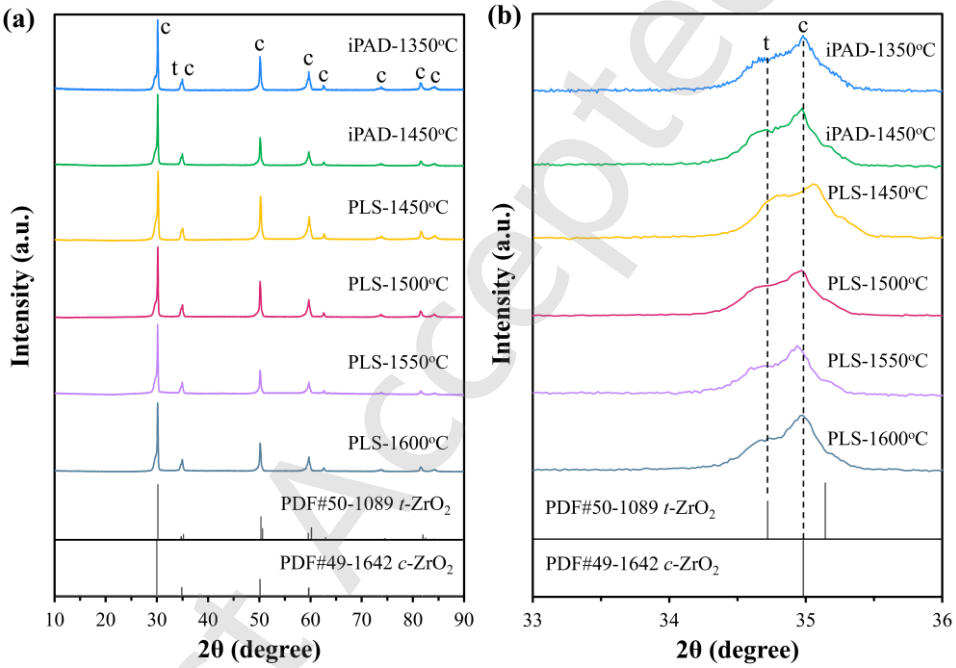


Fig. 5 XRD patterns of the ceramics sintered under different conditions.

Table 1 summarizes the phase fractions, calculated theoretical densities, and lattice-strain-equivalent stress values obtained from a single full-pattern refinement for each processing condition. For the present refinements, R_p ranged from 2.26% to 4.19%, R_{wp} from 3.05% to 5.49%, and χ^2 from 1.74 to 2.96. These indicators, together with the close agreement between the observed and calculated profiles and the absence of pronounced systematic features in the difference curves (Fig. S2), support that the refinement results are highly reliability under the refinement method. For the PLS samples, as the sintering temperature increased from 1450 to 1600 °C, the *t*-ZrO_2 content gradually increased from 69.0 to 76.6 wt%, whereas the *c*-ZrO_2 content decreased from 31.0 to 23.4 wt%. Correspondingly,

Just Accepted

because the theoretical density of *t*-ZrO_2 is lower than that of *c*-ZrO_2, the calculated theoretical density decreased slightly from 6.092 to 6.079 $g \cdot cm^{-3}$. This continuous phase evolution suggests that increasing the PLS temperature promoted structural re-equilibration of the dual-phase 5Y-ZrO_2 ceramics, which may involve enhanced atomic diffusion, local Y^{3+} redistribution, grain-boundary segregation, and adjustment of the *t/c* phase equilibrium [27-29].

Compared with the PLS samples, the pre-sintered and iPAD-treated samples exhibited a different phase-composition evolution. The 1450 ºC pre-sintered ceramic contained 53.6 wt% *t*-ZrO_2 and 46.4 wt% *c*-ZrO_2. After iPAD treatment, the *t*-ZrO_2 content increased to 64.5 wt% at 1350 °C and 62.6 wt% at 1450 ºC, with the corresponding *c*-ZrO_2 contents decreasing to 35.5 and 37.4 wt%, respectively. However, increasing the iPAD temperature from 1350 to 1450 ºC resulted in a slight decrease in the refined *t*-ZrO_2 fraction, in contrast to the continuous increase observed in the PLS series. This difference indicates that the phase evolution of 5Y-ZrO_2 cannot be explained solely by the peak treatment temperature. Instead, the apparent *t/c* phase balance is determined by the combined effects of the initial microstructural state, thermal-pressure history, local Y^{3+} distribution, grain-boundary segregation, oxygen-vacancy distribution, and lattice strain [28,40,60].

Based on the lattice parameters obtained from XRD Rietveld refinement, the lattice-strain-equivalent residual stresses were estimated using the lattice-strain method [54,61]. For the PLS samples, the estimated stress gradually decreased from 1484.0 MPa at 1450 ºC to 1205.0 MPa at 1500 ºC, 972.7 MPa at 1550 ºC, and 931.7 MPa at 1600 ºC. This trend indicates that increasing the PLS temperature promoted atomic diffusion, grain-boundary migration, lattice rearrangement, and stress relaxation. The 1450 ºC pre-sintered ceramic exhibited the highest estimated stress of 1584.2 MPa, whereas the values for the iPAD-1350 ºC and iPAD-1450 ºC samples were 1487.3 and 742.0 MPa, respectively. The marked decrease observed for the iPAD-1450 ºC specimen indicates that the complete iPAD processing route, comprising elevated-temperature isotropic-pressure treatment followed by air annealing, promoted lattice-strain relaxation. Notably, iPAD-1450 ºC exhibited the

Just Accepted

lowest estimated stress but did not possess the highest *t*-ZrO_2 fraction. Therefore, the refined phase fractions cannot be interpreted as being controlled solely by the accumulation or relaxation of residual stress; rather, phase evolution and lattice-strain relaxation represent coupled but distinct structural responses to the processing route.

Because tetragonal and cubic ZrO_2 have closely related crystal structures and substantially overlapping diffraction reflections, the phase-specific peak breadths required for a conventional Williamson-Hall analysis would be highly sensitive to profile deconvolution using the present laboratory XRD data [62-64]. Therefore, the reported stress values are used as comparative lattice-strain-equivalent estimates among specimens measured and refined under identical conditions. The possible contribution of residual stress to the apparent phase fractions should consequently be regarded as a plausible interpretation rather than conclusive evidence. Overall, the results in Table 1 demonstrate that PLS and iPAD produce distinct pathways of phase evolution and lattice-strain relaxation. In particular, iPAD treatment at 1450 °C established the most relaxed lattice state while preserving the characteristic tetragonal-cubic dual-phase structure of 5Y-ZrO_2.

Table 1 XRD Rietveld refinement results and lattice-strain-equivalent residual stress of the ceramics sintered under different conditions

Samples	Theoretical crystalline density		Crystalline phase content (wt%)		Theoretical density	Lattice-strain-equivalent residual stress (MPa)
	t-ZrO_2	*c*-ZrO_2	*t*-ZrO_2	*c*-ZrO_2		
PLS-1450 °C	6.04	6.21	69.0	31.0	6.092	1484.0
PLS-1500 °C			73.4	26.6	6.084	1205.0
PLS-1550 °C			75.9	24.1	6.080	972.7
PLS-1600 °C			76.6	23.4	6.079	931.7
Pre-sintered ceramic-1450 °C			53.6	46.4	6.118	1584.2

Just Accepted

iPAD-1350 ºC			64.5	35.5	6.099	1487.3
iPAD-1450 ºC			62.6	37.4	6.102	742.0

Table 2 summarizes the variations in density and porosity of the 5Y-ZrO_2 ceramics sintered under different conditions. For the PLS samples, as the sintering temperature increased from 1450 to 1500 ºC, the relative density increased from 98.03% to 98.54%, while the apparent porosity decreased from 0.159 ± 0.022% to 0.132 ± 0.022%. This indicates that an appropriate increase in sintering temperature can promote diffusion-driven pore elimination. However, when the temperature was further increased to 1550-1600 ºC, the relative density decreased to 96.84%-97.57%, accompanied by a reduction in apparent porosity. This indicates that excessively high temperatures lead to grain coarsening and the transformation of some open pores into closed pores, thereby not only reducing the measured apparent porosity but also hindering further densification [27,29,65].

The 1450 ºC pre-sintered sample exhibited a relatively low relative density of 96.52% and a high apparent porosity of 1.251 ± 0.001%, indicating that pre-sintering mainly served to close surface-connected pores but was insufficient to achieve full densification. After iPAD treatment, the bulk density increased to approximately 6.03 g cm^{-3}, the relative density reached 98.90% - 98.92%, and the apparent porosity decreased to 0.023 ± 0.023%, which was clearly superior to those of the PLS samples. This demonstrates that the isotropic pressure applied during iPAD can further promote residual pore closure, particle rearrangement, and grain-boundary bonding in addition to high-temperature diffusion, thereby enabling efficient densification under a lower thermal budget [37-39,54].

Combined with the Rietveld refinement results (Table 1), the iPAD-treated samples retained the *t/c* dual-phase structure but did not exhibit systematically higher *t*-ZrO_2 fractions than the PLS samples. Therefore, the principal advantage of iPAD lies in reducing residual porosity and promoting densification rather than in tetragonal-phase enrichment. Overall, iPAD effectively overcomes the densification limitation of PLS and provides an effective route for obtaining highly dense, low-defect PμSL-printed 5Y-ZrO_2 ceramics [15,22,23,37].

Just Accepted

Table 2 Apparent density, bulk density, relative density, and apparent porosity of the ceramics sintered under different conditions

Samples	Apparent density ($g \cdot cm^{-3}$)	Bulk density ($g \cdot cm^{-3}$)	Relative density (%)	Apparent Porosity (%)
PLS-1450 °C	6.027±0.031	5.972±0.040	98.03	0.159±0.022
PLS-1500 °C	6.034±0.040	5.995±0.010	98.54	0.132±0.022
PLS-1550 °C	6.032±0.070	5.888±0.001	96.84	0.070±0.023
PLS-1600 °C	6.057±0.059	5.931±0.002	97.57	0.028±0.028
Pre-sintered ceramic-1450 °C	6.040±0.006	5.905±0.069	96.52	1.251±0.001
iPAD-1350 °C	5.989±0.006	6.033±0.005	98.92	0.023±0.023
iPAD-1450 °C	6.067±0.021	6.035±0.026	98.90	0.023±0.023

3.5 Mechanical properties of the ceramics

Fig. 6 shows the mechanical properties of the ceramics sintered under different conditions. The PLS samples exhibited a non-monotonic variation in flexural strength with increasing sintering temperature (Fig. 6a). The strength increased to a maximum of 785.90 MPa at 1500 °C, but then decreased to 647.26 MPa at 1600 °C. Meanwhile, the fracture toughness showed an overall decreasing trend with increasing PLS temperature (Fig. 6e). The hardness also gradually decreased from 13.48 ± 0.021 to 13.22 ± 0.047 GPa as the sintering temperature increased from 1450 to 1600 °C. In contrast, the iPAD-treated ceramics exhibited superior overall mechanical performance. In particular, the iPAD-1450 °C sample achieved a flexural strength of 951.30±71.05 MPa, a hardness of 13.60 ± 0.069 GPa, and a fracture toughness of 4.06 ± 0.298 $MPa \cdot m^{1/2}$.

Based on the above analysis of the mechanical properties of all ceramic specimens, the PLS-1500 °C and iPAD-1450 °C specimens were selected as representative samples for comparing the overall performance of materials produced by the PLS and iPAD processes under their respective optimized conditions. Under the same indentation load, radial cracks extending from the indentation corners were

Just Accepted

observed in both the PLS-1500 ºC sample (Fig. 6b, c) and the iPAD-1450 ºC sample (Fig. 6f, g). Further high-magnification SEM observation of the cracks in the PLS-1500 ºC ceramic (Fig. 6d) reveals a relatively straight crack propagation path, with both crack length and width significantly larger than those in the iPAD-1450 ºC ceramic (Fig. 6h), and only limited crack branching and deflection (circles in Fig. 6d). This indicates that, under pressureless sintering conditions, crack propagation experiences lower resistance, facilitating the formation of long and wide macroscopic cracks [66], which is consistent with its lower fracture toughness (3.96 ± 0.342 MPa·m$^{1/2}$). In contrast, the crack of iPAD-1450 ºC ceramic (Fig. 6h) exhibit a more slender and compact morphology with a relatively uniform width, accompanied by step-like features and localized crack deflection (circles in Fig. 6h). The overall crack length is shorter and the crack width is narrower. This behavior indicates that the iPAD treatment refines the grain structure and increases densification, thereby significantly enhancing resistance to crack propagation, which is consistent with its higher fracture toughness (4.06 ± 0.298 MPa·m$^{1/2}$).

The enhanced mechanical properties of the iPAD-treated ceramics can be attributed primarily to improved densification and microstructural uniformity. First, iPAD effectively eliminated residual pores that were difficult to remove by diffusion-controlled PLS, increasing the relative density to approximately 98.90%-98.92% (Table 2). This high degree of densification reduces defect-induced stress concentrations and provides the structural basis for improved strength. Notably, iPAD-1450 ºC contained a lower *t*-ZrO_2 fraction than PLS-1500 ºC (62.6 versus 73.4 wt%) but nevertheless exhibited higher flexural strength and slightly higher fracture toughness. This comparison indicates that the mechanical improvement cannot be attributed to an increase in the tetragonal-phase fraction. Instead, residual-pore elimination, tighter grain-boundary bonding, and a more uniform grain-size distribution reduced the probability of crack initiation and increased resistance to crack propagation. By contrast, excessive PLS temperatures promoted grain coarsening and pore evolution, leading to deterioration of the mechanical performance above 1500 ºC [27,30,65].

Just Accepted

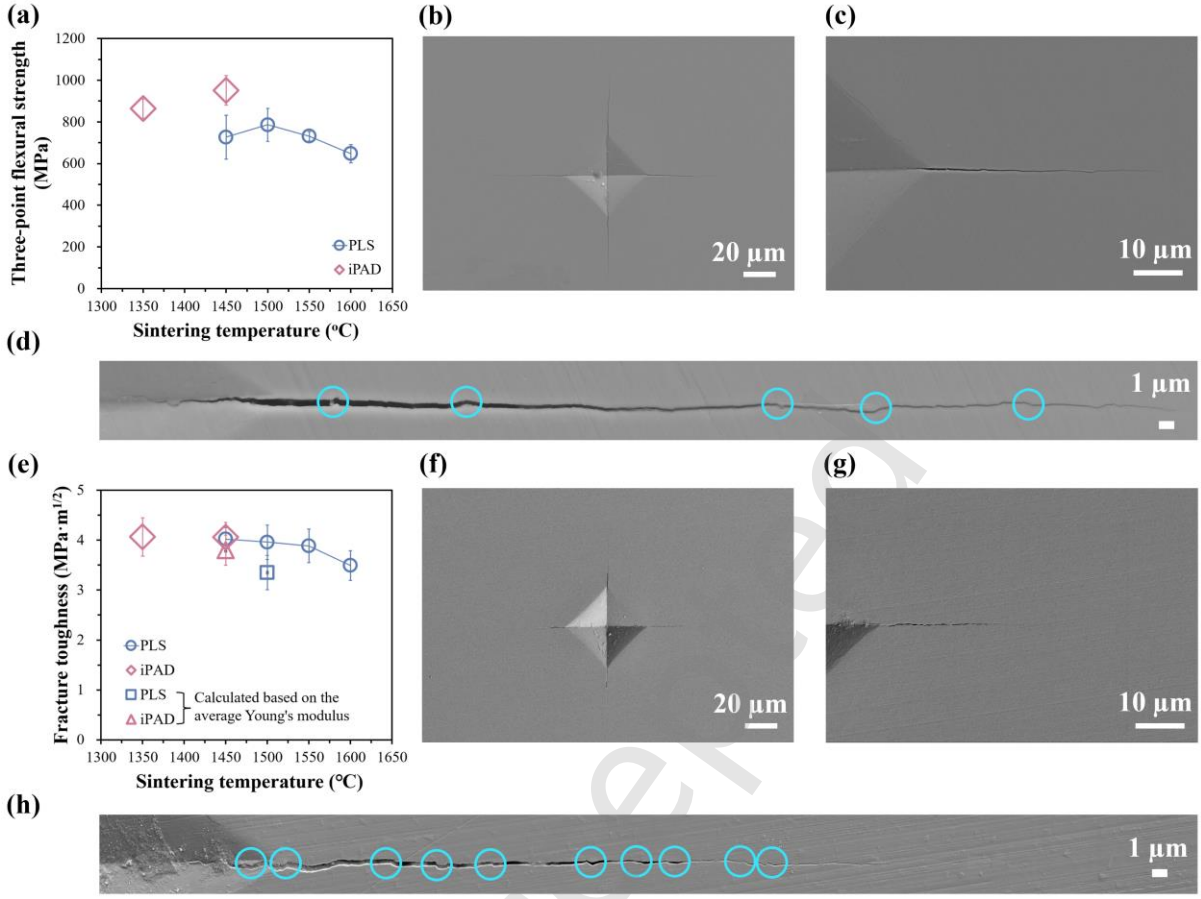


Fig. 6 Mechanical properties and indentation morphology of ceramics sintered under different conditions: (a) three-point flexural strength diagram; (b) representative indentation morphology of PLS-1500 °C sample; (c, d) representative crack propagation morphology of PLS-1500 °C sample; (e) fracture toughness diagram (the square and triangle symbols represent the fracture toughness values of the PLS-1500 °C and iPAD-1450 °C samples, respectively, calculated using the mean Young's moduli obtained from nanoindentation measurements); (f) representative indentation morphology of iPAD-1450 °C sample; (g, h) representative crack propagation morphology of iPAD-1450 °C sample.

3.6 Ultra-thin zirconia ceramic veneers

Fig. 7 compares the surface morphologies and optical properties of 80 μm-thick square zirconia ceramic plate specimens sintered under different conditions. The macroscopic photographs (Fig. 7a) show that the iPAD-treated samples exhibit higher translucency than the PLS samples, as evidenced by the clearer visibility of the black background stripes. Surface roughness measurements (Fig. 7b) further reveal that the PLS samples have a higher roughness value of 0.49 ± 0.05 μm, whereas the

iPAD-treated samples show a much smoother surface with a roughness of 0.20 ± 0.02 μm. This reduced surface roughness is expected to decrease interfacial reflection and scattering, thereby contributing to improved optical transmission. The contrast ratio (CR), an important parameter for evaluating the translucency of dental ceramics, also confirms this improvement. A lower CR value indicates higher translucency. As shown in Fig. 7c, the CR of the iPAD-treated samples is 0.65 ± 0.03, lower than that of the PLS samples at 0.73 ± 0.02. The reflectance spectra measured against black (Y_{black}) and white (Y_{white}) backgrounds are shown in Fig. 7d and e. Materials containing abundant internal scattering centers, such as residual pores, generally exhibit stronger light reflection during transmission, particularly against a black background [6,7,67,68]. Across the visible wavelength range of 380-780 nm, the iPAD-treated samples show consistently lower black-background reflectance than the PLS samples, indicating reduced internal scattering and improved light transmission.

The total transmittance spectra (Fig. 7f) further demonstrate the enhanced optical performance of the iPAD-treated ceramics. For both groups, transmittance increases gradually with wavelength, while the iPAD-treated samples maintain higher transmittance throughout the visible range. At 555 nm, where the human eye is most sensitive, the transmittance of the iPAD-treated samples reaches 56.15 ± 1.11%, compared with 46.52 ± 0.52% for the PLS samples, corresponding to an increase of ~10%.

A higher cubic-phase fraction is generally favorable for zirconia translucency because of its lower optical anisotropy. The corrected Rietveld results show that iPAD-1450 ºC contained a higher *c*-ZrO_2 fraction than PLS-1500 ºC (37.4 versus 26.6 wt%), which is directionally consistent with its higher total transmittance at 555 nm (56.15 ± 1.11% versus 46.52 ± 0.52%). However, the contribution of phase composition cannot be quantitatively separated from the simultaneous microstructural changes induced by iPAD. The most direct microstructural evidence identifies the reduction in residual pores and pore-related interfaces as a principal factor: compared with PLS-1500 ºC, iPAD-1450 ºC reduced the apparent porosity from 0.132 ± 0.022% to 0.023 ± 0.023% and markedly decreased intergranular pores and grain-boundary voids. Because of the large refractive-index mismatch between zirconia and

Just Accepted

gas-filled pores, even a small residual-pore population can cause substantial visible-light scattering [6,7,67,68]. The lower black-background reflectance of the iPAD sample further supports the reduction in internal scattering. Therefore, the improved translucency is attributed to the combined effects of a higher cubic-phase fraction, residual-pore elimination, microstructural homogenization, and reduced surface roughness, with pore elimination representing the principal directly supported microstructural contribution.

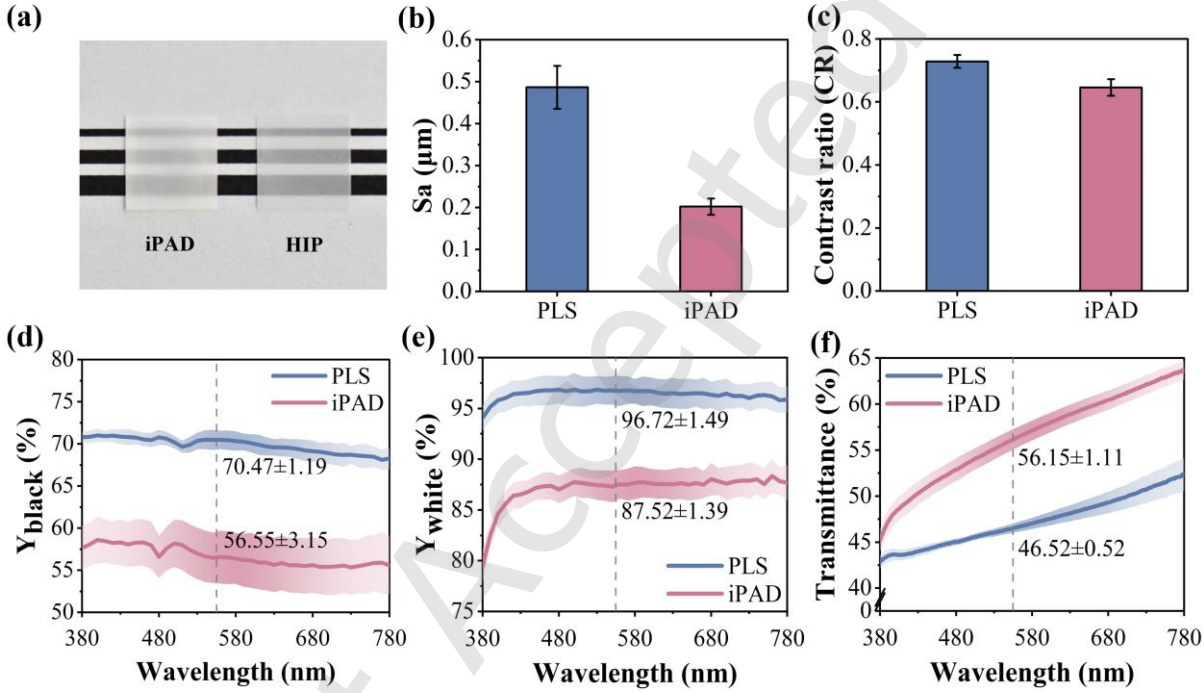


Fig. 7 Optical properties of 80 μm-thich 5Y-ZrO_2 ceramic plates sintered under different conditions: (a) optical photographs, (b) surface roughness, (c) contrast ratio, (d) reflectance spectra measured against a black background, (e) reflectance spectra measured against a white background, and (f) total transmittance spectra.

An ultrathin zirconia veneer with a thickness of approximately 80 μm was designed for the maxillary right central incisor and fabricated by PμSL printing (Fig. 8a). After sintering, the iPAD-treated veneer exhibited higher translucency than the PLS veneer, as indicated by the clearer visibility of the background features (Fig. 8b). The dimensional accuracy of the veneers was evaluated by comparing the scanned data with the original CAD model (Fig. 8c). In the deviation color maps, red / yellow regions represent positive deviations, where the scanned surface protrudes outward relative to the CAD

Just Accepted

model, whereas cyan / blue regions indicate negative deviations, where the scanned surface is recessed. The deviation maps of both veneers are dominated by green regions, corresponding to deviations within 20 μm, demonstrating that the iPAD-treated veneers maintained high manufacturing accuracy comparable to that of PLS veneers. The fracture resistance of the ultrathin veneers was further evaluated by mechanical loading tests (Fig. 8d, e). The ultimate fracture load increased from 12.8 ± 1.9 N for the PLS veneers to 17.3 ± 2.1 N for the iPAD-treated veneers, representing an improvement of approximately 35%. These results demonstrate that the iPAD enhances the fracture resistance of ultrathin zirconia veneers while preserving high dimensional accuracy, supporting its potential for minimally invasive dental restorations.

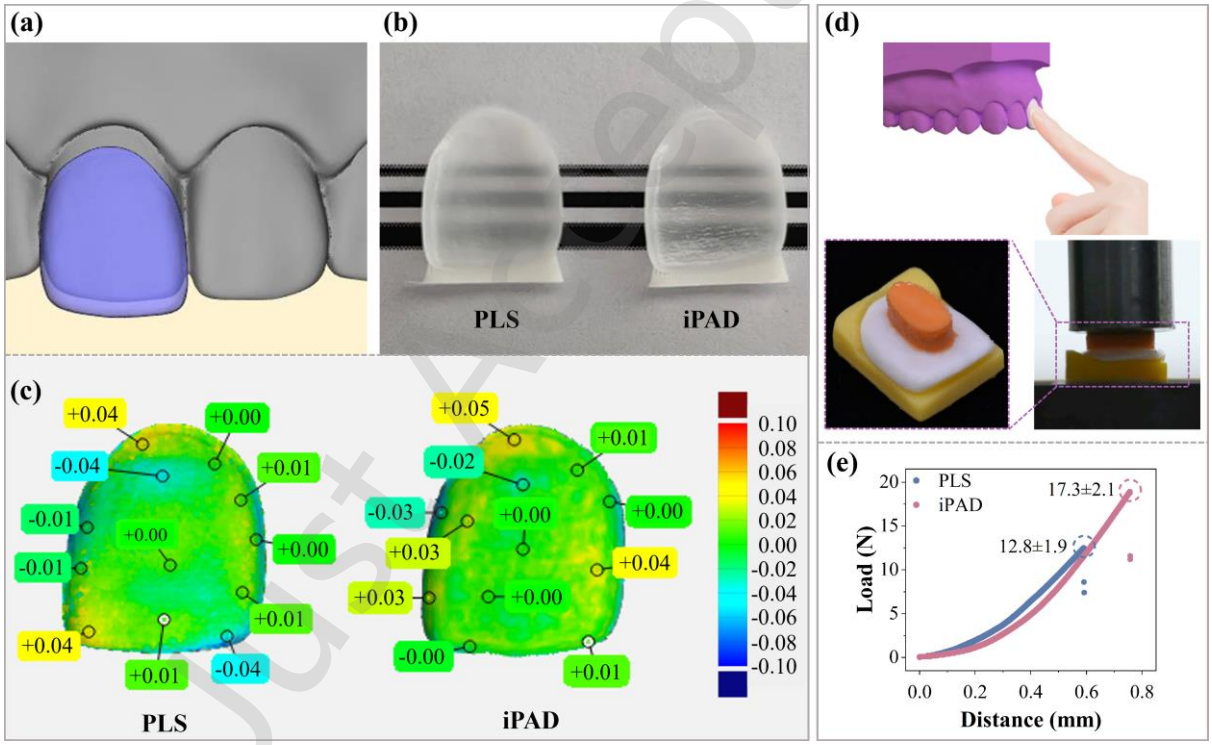


Fig. 8 Translucency, dimensional accuracy, and fracture resistance of ultrathin zirconia veneers. (a) Design and CAD model of ultrathin zirconia veneer for the maxillary right central incisor. (b) Optical photographs of PLS- and iPAD-treated veneers showing translucency differences. (c) Representative deviation color maps between the scanned veneer data and the CAD model. (d) Schematic and photograph of the mechanical loading test. (e) Ultimate fracture loads of PLS- and iPAD-treated veneers.

Just Accepted

To benchmark the overall performance of the present material, its properties were compared with those of recently reported 3D-printed dental zirconia and HIP-densified zirconia ceramics, as summarized in Tables S2 and S3. The PμSL-iPAD 5Y-ZrO_2 developed in this study exhibited a three-point flexural strength of 951.30 ± 71.05 MPa, which was higher than the values reported for most compositionally comparable 3D-printed 4Y-PSZ and 5Y-PSZ ceramics. Its hardness of 13.60 ± 0.07 GPa and fracture toughness of 4.06 ± 0.30 MPa·$m^{1/2}$ were also competitive with the corresponding reported values. Conventional HIP can produce nearly fully dense zirconia with high transmittance; however, these results were mainly obtained from pressed, optically polished, millimeter-thick 3Y-TZP or cubic-rich 8YSZ specimens, which differ substantially from the present ultrathin 5Y-ZrO_2 in composition and testing conditions. Although these differences preclude strict numerical ranking, the present strategy simultaneously achieved a relative density of 98.90%, a total transmittance of 56.15% at 555 nm, and high mechanical reliability in unpolished components approximately 80 μm thick, demonstrating a favorable balance among additive-manufacturing capability, densification, mechanical performance, and visible-light transmittance.

4 Discussion

The nanoscale phase distribution and local elemental homogeneity of the PLS-1500 ºC and iPAD-1450 ºC ceramics were further investigated to determine whether different densification routes induced microstructural or compositional heterogeneity. For this purpose, electron-transparent lamellae were prepared by FIB thinning and subsequently characterized by TEM (Fig. 9). The low-magnification TEM image of the PLS-1500 ºC ceramic (Fig. 9a) shows a certain degree of microstructural heterogeneity, with locally distributed grains of different contrasts and sizes, as well as obvious pores. The high-magnification TEM image (Fig. 9b) further reveals relatively nonuniform grain arrangement in the PLS sample, with pronounced contrast variations in some grain-boundary regions and grain boundaries with a certain thickness, suggesting that residual defects, local stresses, or compositional fluctuations may still exist after pressureless sintering. Clear lattice fringes can be observed in the

Just Accepted

HRTEM image (Fig. 9c). Combined with the corresponding SAED patterns (Fig. 9d, e), the coexistence of *t*-ZrO_2 and *c*-ZrO_2 phases in the PLS-1500 ºC ceramic is confirmed, which is consistent with the XRD results (Fig. 5). In contrast, the iPAD-1450 ºC ceramic exhibits a denser and more homogeneous microstructure. Its low-magnification TEM image (Fig. 9f) shows a more uniform overall internal contrast, with no obvious large pores or loose regions. The high-magnification TEM image (Fig. 9g) further indicates tighter intergranular bonding in the iPAD sample, with thinner and straighter grain boundaries and more continuous grain-boundary profiles. The HRTEM image (Fig. 9h) and SAED patterns (Fig. 9i, j) also confirm the coexistence of *t*-ZrO_2 and *c*-ZrO_2 phases, indicating that iPAD treatment did not introduce new impurity phases, but improved the local microstructural uniformity while maintained the dual-phase structure of 5Y-ZrO_2.

The Y elemental line-scan and mapping results in Fig. 9(k-n) show local fluctuations in the Y signal within the selected fine-grain regions of both the PLS-1500 ºC and iPAD-1450 ºC ceramics. Although a slightly lower local Y signal is visible in the selected region of the iPAD sample, the limited sampling and the spatial and quantitative resolution of TEM-EDS do not allow this difference to be reliably attributed to the iPAD treatment. Therefore, within the sampling statistics and resolution of the present TEM-EDS measurements, no discernible iPAD-induced change in the Y distribution was observed.

Just Accepted

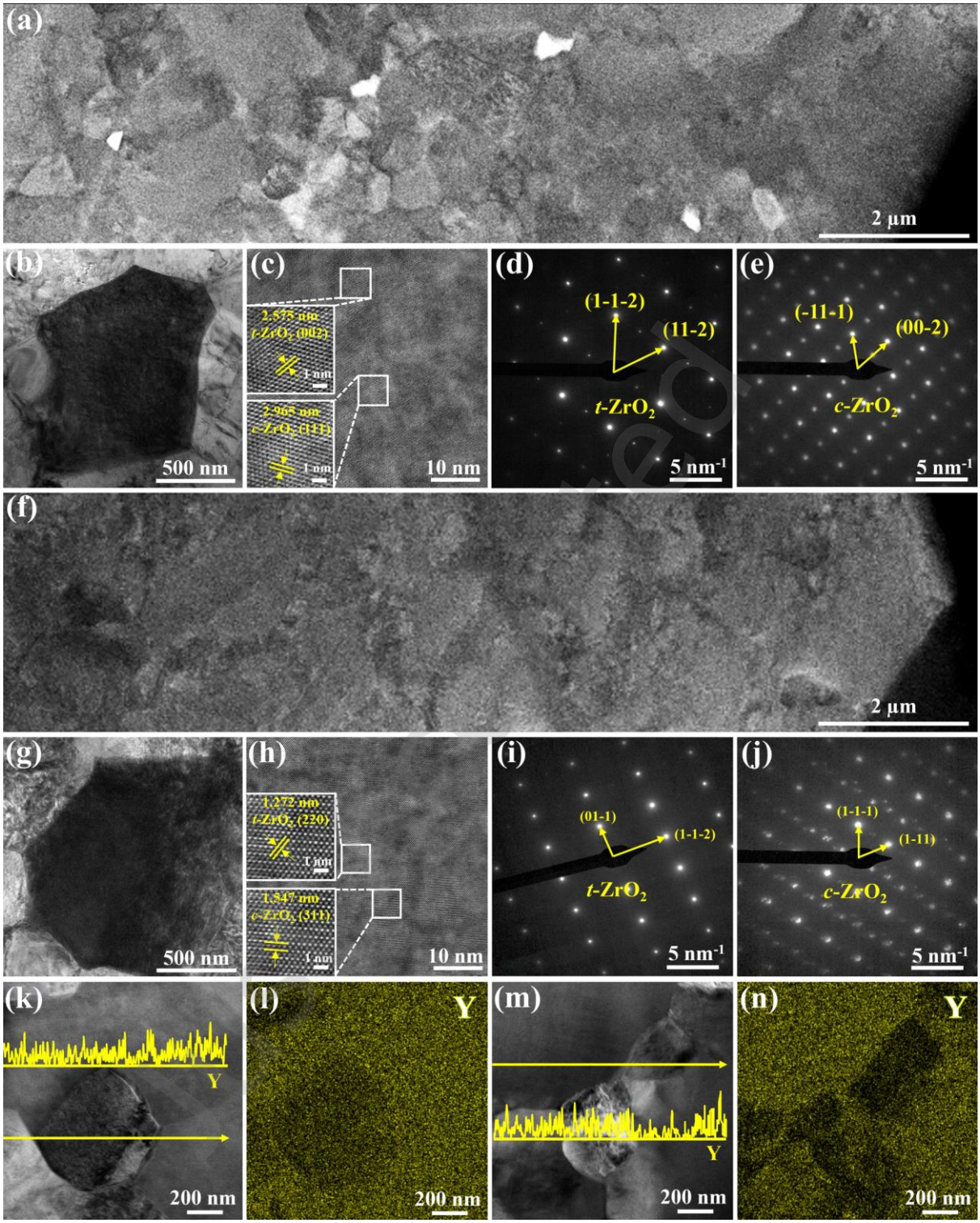


Fig. 9 TEM images and elemental distribution maps of the PLS-1500 °C and iPAD-1450 °C ceramics. Low-magnification TEM image (a), high-magnification TEM image (b), HRTEM image (c), and selected-area electron diffraction (SAED) patterns (d, e) of the PLS-1500 °C ceramic; low-magnification TEM image (f), high-magnification TEM image (g), HRTEM image (h), and SAED patterns (i, j) of the iPAD-1450 °C ceramic.

Y elemental line-scan analyses of the PLS-1500 ºC (k) and iPAD-1450 ºC (m) ceramics; Y elemental mapping images of the PLS-1500 ºC (l) and iPAD-1450 ºC (n) ceramics.

To elucidate the influence of the PLS and iPAD processes on the chemical states of 5Y-ZrO_2 ceramics, X-ray photoelectron spectroscopy (XPS) analysis was performed on the fresh fracture surfaces of the PLS-1500 ºC and iPAD-1450 ºC specimens. The results confirm the presence of Zr 3s (~270 eV), Y 3d (~156 eV), and O 1s (~532 eV) in both samples (Fig. 10a). Fig. 10b displays the high-resolution Zr 3d spectra with in the 178-188 eV binding energy range, where both ceramics exhibit a typical doublet structure. However, the peaks corresponding to Zr $3d_{5/2}$ (~182 eV) and Zr $3d_{3/2}$ (~184 eV) in the iPAD-1450 ºC ceramic is sharper and more intense, with a narrower full width at half maximum (FWHM) compared to those of the PLS ceramic. This broadening suggests that the chemical environment of Zr in the PLS samples undergoes slight distortion, likely driven by a higher density of oxygen vacancies or residual lattice stress [40,69,70]. Deconvolution of the high-resolution Y 3d spectra (Fig. 10c) reveals a characteristic peak at 152.7-153.3 eV in both ceramics, corresponding to a low-binding-energy state of Y^{3+} coordinated with neighboring oxygen vacancies. Strikingly, the relative concentration of this peak is only 0.66% in the iPAD-1450 ºC ceramic, whereas it surges to 8.41% in the PLS-1500 ºC ceramic (Table 3). This pronounced coordination between Y^{3+} and oxygen vacancies in the PLS-1500 ºC sample indirectly reflects a substantially higher vacancy concentration. This conclusion is further corroborated by the high-resolution O 1s spectra (Fig. 10d), which delineate lattice oxygen, oxygen-vacancy-related oxygen, and adsorbed oxygen. The PLS-1500 ºC ceramic contains higher relative fractions of both oxygen-vacancy-related and adsorbed oxygen, indicating that the absence of external pressure during PLS facilitates the loss of lattice oxygen, thereby generating more oxygen vacancies and active sites for surface adsorption [40,41,69].

Table 3 Relative contents of Y and O species determined by XPS in iPAD-1450 ºC and PLS-1500 ºC ceramics.

Elements	Binding energy (eV)	Assignment	Percentage (%)	
			iPAD-1450 ºC	PLS-1500 ºC
Y	158.9	Y $3d_{5/2}$	45.66	42.16

Just Accepted

	156.9	Y $3d_{3/2}$	53.68	49.43
	152.7-153.3	Y^{3+}_V_O	0.66	8.41
O	529.7-529.8	O_{lat}	75.51	64.40
	531.5	O vacancy	20.45	29.35
	532.7	O_{ads}	4.04	6.25

To validate these XPS findings, EPR spectroscopy was employed (Fig. 10e and Fig. 10f). A distinct absorption resonance at g = 2.0039, corresponding to unpaired electrons trapped in oxygen vacancies, appears in both spectra. However, the signal intensity of iPAD-1450 ºC ceramic is markedly weaker than that of the PLS-1500 ºC ceramic, pointing to a much lower oxygen vacancy concentration. In contrast, the PLS-1500 ºC sample exhibits a higher defect density, which may involve the localized aggregation of these defects [42,69]. Quantitative analysis confirms that under identical acquisition and normalization conditions, the relative intensity of the oxygen-vacancy-related EPR signal in the PLS ceramic was 38.8 times that in the iPAD ceramic. Overall, these results demonstrate that the ceramic produced by the complete iPAD route contained fewer oxygen-vacancy-related defects than the PLS ceramic. A lower population of oxygen-vacancy-related defects may reduce local lattice distortion and defect-related optical absorption [40,70]. Nevertheless, the contribution of defect chemistry to the improved translucency is considered secondary to the elimination of residual pores and pore-related scattering interfaces, which are regarded as the dominant sources of optical scattering in the present ceramics [65,66]. Similarly, the independent contribution of oxygen-vacancy-related defects to mechanical reliability cannot be separated from the concurrent changes in porosity, grain-boundary bonding, and microstructural uniformity. Because the iPAD specimens underwent subsequent heat treatment in air, the observed reduction in oxygen-vacancy-related defects cannot be assigned to pressure alone. Instead, it should be interpreted as the combined result of pressure-assisted processing under Ar and subsequent air annealing, with the latter promoting reoxidation and recovery of oxygen stoichiometry. XPS of freshly exposed internal fracture surfaces probes near-surface chemical states associated with oxygen deficiency, whereas EPR samples a larger volume and

Just Accepted

selectively detects paramagnetic electron-trapping oxygen-vacancy-related centers. The lower XPS defect-related components and weaker EPR signal near g = 2.0039 therefore consistently indicate a lower relative abundance of oxygen-vacancy-related defects in the ceramic produced by the complete iPAD route, although neither technique provides an absolute vacancy concentration.

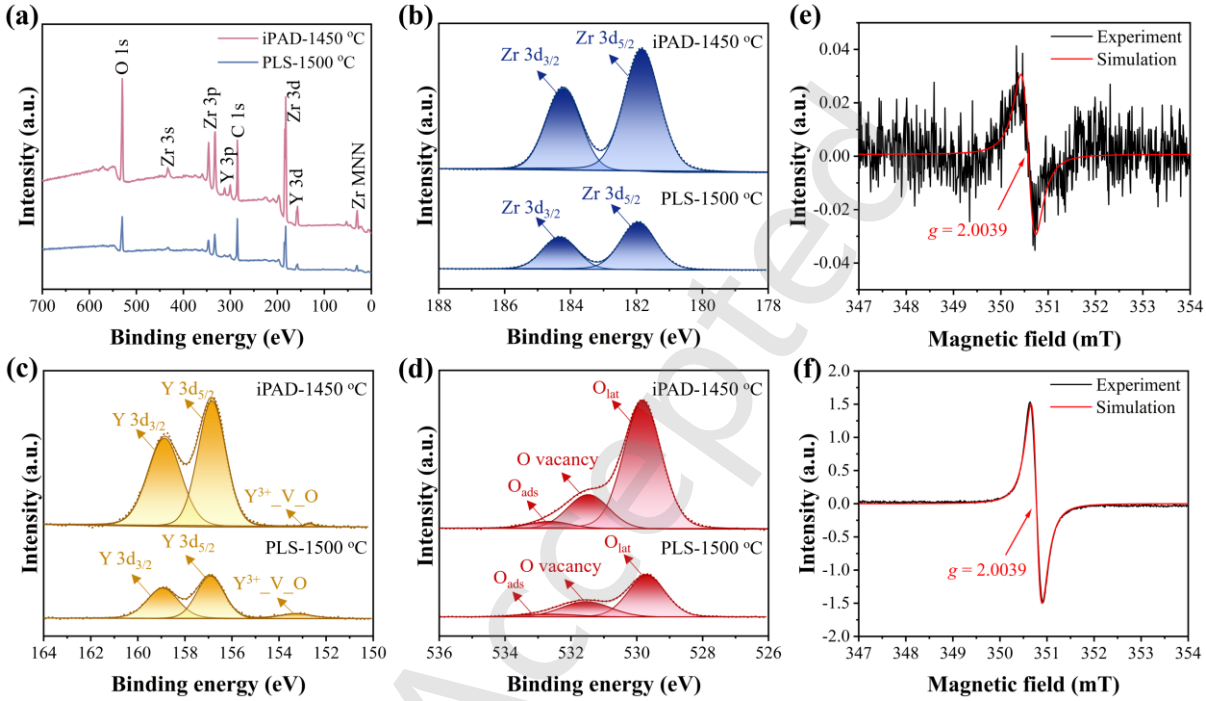


Fig. 10 XPS spectra of the iPAD-1450 °C and PLS-1500 °C ceramics: survey spectra (a), Zr 3d (b), Y 3d (c), and O 1s (d); EPR spectra of iPAD-1450 °C (e) and PLS-1500 °C (f).

To evaluate the effect of different densification routes on the nanoscale mechanical response and microstructural uniformity of 5Y-ZrO_2 ceramics, high-throughput nanoindentation tests were performed on the PLS-1500 °C and iPAD-1450 °C samples. For each sample, a 100 × 100 indentation array was applied with an interval of 2 μm between adjacent indents, covering a total area of approximately 200 μm × 200 μm [71]. For the PLS-1500 °C ceramic, the 10000 load-displacement curves exhibit pronounced dispersion (Fig. 11a), indicating heterogeneous local deformation behavior. The post-indentation *in-situ* SPM image shows nonuniform indentation depths, with numerous darker regions corresponding to deeper indents (Fig. 11b). The hardness histogram displays a relatively broad distribution with a low-hardness tail (Fig. 11c), while the Young's modulus histogram also shows a

Just Accepted

wide distribution range (Fig. 11d). Consistently, the spatial distribution maps of hardness and Young's modulus reveal pronounced mechanical heterogeneity, with scattered low-value regions across the tested area (Fig. 11e and f). In contrast, the iPAD-1450 ºC ceramic shows more concentrated load-displacement curves (Fig. 11g), suggesting a more uniform nanoscale deformation response. The corresponding SPM image exhibits fewer deep indentation regions and a more homogeneous surface response after indentation (Fig. 11h). Compared with the PLS sample, the iPAD-treated ceramic shows a narrower hardness distribution (Fig. 11i) and a more concentrated Young's modulus distribution (Fig. 11j). The hardness and Young's modulus maps further confirm the improved spatial uniformity of the iPAD-treated ceramic, with fewer mechanically weak regions and a more continuous distribution of medium-to-high values (Fig. 11k and l). These results demonstrate that iPAD significantly improves the nanoscale mechanical uniformity of 5Y-ZrO_2 ceramics. By reducing residual porosity, suppressing defect-induced stress concentration, and enhancing microstructural homogeneity, the iPAD-treated ceramic exhibits more consistent resistance to both plastic and elastic deformation during nanoindentation. This improved local mechanical uniformity provides direct evidence for the role of iPAD in enhancing the mechanical reliability of printed zirconia ceramics.

Averaging the 10000 local measurements yielded Young's moduli of 144.569 and 186.193 GPa for the PLS-1500 ºC and iPAD-1450 ºC samples, respectively. Because the indentation-derived fracture toughness calculated using Eq. (5) is proportional to $E^{0.4}$, substitution of these mean moduli reduced the corresponding K_{Ic} values from 3.96 to 3.35 MPa·m$^{1/2}$ for the PLS sample and from 4.06 to 3.80 MPa·m$^{1/2}$ for the iPAD sample, corresponding to decreases of approximately 15.4% and 6.4%, respectively. These results indicate that the absolute magnitude of the indentation-derived fracture toughness is sensitive to the selected modulus and that the lower local modulus and greater mechanical heterogeneity of the PLS sample produce a larger correction; nevertheless, the iPAD sample retains the higher toughness under both calculation approaches, confirming the robustness of the qualitative comparison.

Just Accepted

Overall, the enhanced performance of the iPAD-treated ceramics arises from the synergistic regulation of densification, defect chemistry, and microstructural uniformity enabled by the PμSL-presintering-iPAD strategy. Under elevated temperature and isotropic gas pressure, iPAD promotes residual pore closure and particle rearrangement, resulting in markedly improved densification and reduced porosity. This dense microstructure minimizes structural defects that can serve as crack-initiation sites and light-scattering centers, thereby providing a fundamental basis for the simultaneous improvement of mechanical reliability and optical translucency.

Although the present study demonstrates the improved material properties, manufacturing accuracy, and initial structural feasibility of PμSL-iPAD-fabricated ultrathin zirconia veneers, long-term clinical performance involves more complex interactions within the tooth-cement-veneer system. The current mechanical evaluation primarily focused on intrinsic ceramic properties and veneer-level fracture resistance under clinically relevant handling conditions. Future studies should further investigate restoration-level durability through cyclic fatigue and thermocycling under simulated oral environments, considering the combined effects of repeated occlusal loading, temperature fluctuations, moisture exposure, adhesive-interface degradation, and supporting tooth structures. Such investigations, together with ongoing clinical follow-up, will be important for establishing the long-term functional reliability and clinical indications of ultrathin zirconia veneers.

Just Accepted

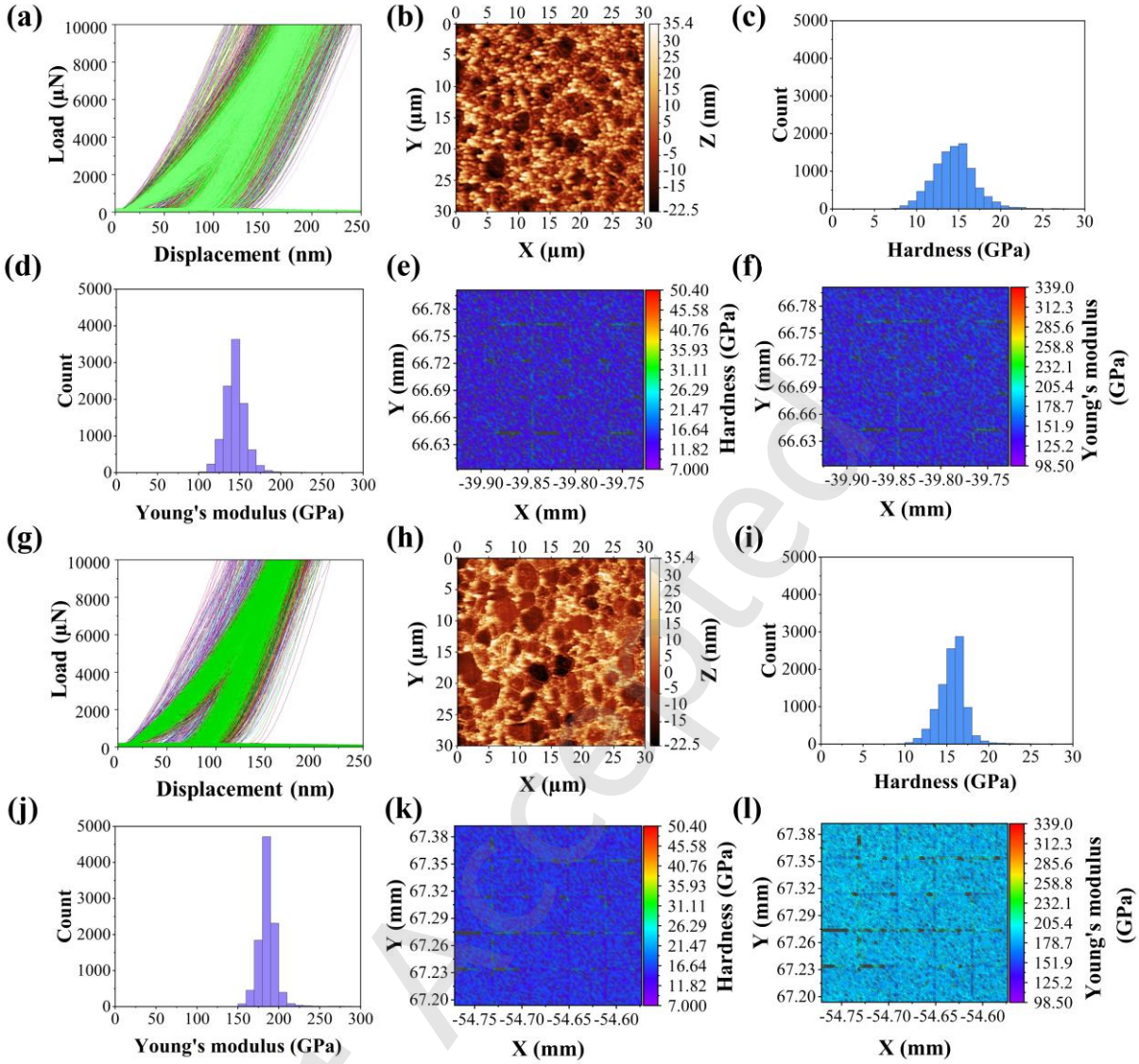


Fig. 11 Nanoindentation characterization of the PLS-1500 ºC and iPAD-1450 ºC 5Y-ZrO_2 ceramics. (a-c) Load-displacement curves, post-indentation SPM image, and hardness distribution histogram of the PLS-1500 ºC ceramic; (d-f) Young's modulus distribution histogram, hardness spatial distribution map, and Young's modulus spatial distribution map of the PLS-1500 ºC ceramic; (g-i) load-displacement curves, post-indentation SPM image, and hardness distribution histogram of the iPAD-1450 ºC ceramic; (j-l) Young's modulus distribution histogram, hardness spatial distribution map, and Young's modulus spatial distribution map of the iPAD-1450 ºC ceramic.

5 Conclusions

This study demonstrates that the PμSL-pre-sintering-iPAD strategy is an effective route for fabricating ultrathin 5Y-ZrO_2 dental ceramics with high mechanical reliability and favorable esthetic properties.

Just Accepted

The underlying mechanism responsible for the improved performance is that isotropic pressure applied at elevated temperature accelerates the shrinkage and closure of residual pores by promoting pressure-assisted mass transport, grain-boundary migration, and high-temperature creep, while strengthening intergranular contact and grain-boundary bonding. Consequently, a dense and homogeneous microstructure with a relative density of 98.90% and an apparent porosity of only 0.023% was obtained. Meanwhile, pressure-assisted densification, together with oxygen re-equilibration during the subsequent heat treatment in air, reduced oxygen-vacancy-related defect states. The reduction in residual pores and weak grain boundaries decreased local stress concentrations and the probability of crack initiation, whereas the more uniform grain-size distribution and stronger grain-boundary bonding increased the resistance to crack propagation. As a result, the iPAD-1450 ^{o}C ceramic achieved a flexural strength of 951.30 ± 71.05 MPa and exhibited a more spatially uniform nanoscale mechanical response. In addition, the reduction in internal pores decreased light scattering caused by refractive-index mismatch, while the decrease in surface roughness from 0.49 to 0.20 μm further reduced surface reflection and diffuse scattering, thereby increasing the transmittance at 555 nm from 46.52% to 56.15%. The synergistic effects of densification, defect regulation, and microstructural homogenization ultimately enhanced the load-bearing capacity of the approximately ~80 μm veneers, increasing their fracture load from 12.8 ± 1.9 to 17.3 ± 2.1 N while maintaining high manufacturing accuracy. Therefore, by establishing a clear mechanistic pathway of "pressure-assisted densification-defect reduction and grain-boundary strengthening-enhancement of mechanical and optical performance," this strategy provides a viable route for the digital fabrication of highly reliable, minimally invasive ultrathin zirconia restorations. Beyond monolithic ultrathin veneers, the PμSL-pre-sintering-iPAD strategy may be extended to multilayered, controlled-porosity, and functionally graded restorations with spatially tailored compositions, microstructures, translucency, and mechanical properties. Future studies should establish structure-specific temperature-pressure-time windows and

Just Accepted

clarify how pressure-assisted densification interacts with differential shrinkage, interfacial stress, and the preservation of designed pore networks or compositional gradients.

Funding

This work was supported by the National Key R&D Program of China (2023YFB4605400), the National Science Foundation of China (52575325), the Beijing Nova Program (20230484337 & 20240484545), the Beijing Natural Science Foundation (2252060), and the Non-profit Central Research Institute Fund of Chinese Academy of Medical Sciences (2023-PT320-09).

Author contributions

Wenhua Tong: Methodology, Investigation, Data curation, Formal analysis, Visualization, Writing - original draft. **Yanru Shen**: Methodology, Investigation, Data curation, Formal analysis, Visualization, Writing - original draft. **Pengjie Zhang:** Methodology, Investigation. **Chen Yang:** Resources. **Ying Jiang:** Resources. **Feng Wang:** Resources. **Suwei Dai:** Methodology, Investigation. **Shuyi Huang:** Methodology, Investigation. **Zhankun Pan:** Resources. **Jinhua Li:** Resources. **Weiwei Li:** Methodology, Investigation. **Yongsheng Zhou：** Resources, Funding acquisition. **Yuchun Sun:** Conceptualization, Resources, Supervision, Funding acquisition. **Lida Che:** Resources, Project administration. **Xiang Wang:** Supervision, Resources, Project administration, Methodology, Investigation, Funding acquisition, Conceptualization, Writing - review & editing.

Availability of data and materials

The data that support the findings of this study are available from the corresponding author upon reasonable request.

Just Accepted

Competing interests

The authors declare that they have no known competing financial interests or personal relationships that could have appeared to influence the work reported in this paper.

References

[1] Zhang Y, Lawn BR. Novel zirconia materials in dentistry. *J Dent Res* 2018, **97**: 140-147.

[2] Piconi C, Maccauro G. Zirconia as a ceramic biomaterial: A review. *Biomaterials* 1999, **20**: 1-25.

[3] Chevalier J, Gremillard L, Virkar AV, *et al*. The tetragonal-monoclinic transformation in zirconia: Lessons learned and future trends. *J Am Ceram Soc* 2009, **92**: 1901-1920.

[4] Zarone F, Di Mauro MI, Ausiello P, *et al*. Current status on lithium disilicate and zirconia: A narrative review. *BMC Oral Health* 2019, **19**: 134.

[5] Zhang F, Reveron H, Spies BC, *et al*. Trade-off between fracture resistance and translucency of zirconia and lithium-disilicate glass ceramics for monolithic restorations. *Acta Biomater* 2019, **91**: 24-34.

[6] Kolakarnprasert N, Kaizer MR, Kim DK, *et al*. New multi-layered zirconias: Composition, microstructure and translucency. *Dent Mater* 2019, **35**: 797-806.

[7] Pereira GKR, Guilardi LF, Dapieve KS, *et al*. Mechanical reliability, fatigue strength and survival analysis of new polycrystalline translucent zirconia ceramics for monolithic restorations. *J Mech Behav Biomed Mater* 2018, **85**: 57-65.

[8] Baldissara P, Wandscher VF, Marchionatti AME, *et al*. Translucency of IPS e.max and cubic zirconia monolithic crowns. *J Prosthet Dent* 2018, **120**: 269-275.

[9] Blatz MB, Vonderheide M, Conejo J. The effect of resin bonding on long-term success of high-strength ceramics. *J Dent Res* 2018, **97**: 132-139.

[10] Miyazaki T, Nakamura T, Matsumura H, *et al*. Current status of zirconia restoration. *J Prosthodont Res* 2013, **57**: 236-261.

Just Accepted

[11] Lan TH, Wang CH, Chen KK, *et al*. Milling properties of low temperature sintered zirconia blocks for dental use. *Mater Sci Eng C* 2017, **73**: 692-699.

[12] Schriwer C, Skjold A, Gjerdet NR, *et al*. Monolithic zirconia dental crowns. Internal fit, margin quality, fracture mode and load at fracture. *Dent Mater* 2017, **33**: 1012-1020.

[13] Malallah AD, Hasan NH. Thickness and yttria percentage influences the fracture resistance of laminate veneer zirconia restorations. *Clin Exp Dent Res* 2022, **8**: 1413-1420.

[14] Alghazzawi TF. Advancements in CAD/CAM technology: Options for practical implementation. *J Prosthodont Res* 2016, **60**: 72-84.

[15] Chen ZW, Li ZY, Li JJ, *et al*. 3D printing of ceramics: A review. *J Eur Ceram Soc* 2019, **39**: 661-687.

[16] Zocca A, Colombo P, Gomes CM, *et al*. Additive manufacturing of ceramics: Issues, potentialities, and opportunities. *J Am Ceram Soc* 2015, **98**: 1983-2001.

[17] Halloran JW. Ceramic stereolithography: Additive manufacturing for ceramics by photopolymerization. *Annu Rev Mater Res* 2016, **46**: 19-40.

[18] Khanlar LN, Rios AS, Tahmaseb A, *et al*. Additive manufacturing of zirconia ceramic and its application in clinical dentistry: A review. *Dent J* 2021, **9**: 104.

[19] Tien C, Jean C, Poupaud L, *et al*. Enhancing dental model accuracy through optimized vat photopolymerization additive manufacturing parameters. *Addit Manuf Lett* 2025, **13**: 100278.

[20] Shen W, Wang GQ, Wang SR, *et al*. Designing and vat photopolymerization 3D printing of glass ceramic/zirconia composites functionally gradient ceramics for dental restorations. *Ceram Int* 2025, **51**: 4441-4452.

[21] Chen A, Li K, Li YJ, *et al*. Occlusion-activated autonomous piezoelectric implants for adaptive prevention of peri-implantitis. *Nat Commun* 2026, **17**: 5017.

[22] Osman RB, van der Veen AJ, Huiberts D, *et al*. 3D-printing zirconia implants; a dream or a reality? An in-vitro study evaluating the dimensional accuracy, surface topography and mechanical properties

Just Accepted

of printed zirconia implant and discs. *J Mech Behav Biomed Mater* 2017, **75**: 521-528.

[23] Coppola B, Schmitt J, Lacondemine T, *et al*. Digital light processing stereolithography of zirconia ceramics: Slurry elaboration and orientation-reliant mechanical properties. *J Eur Ceram Soc* 2022, **42**: 2974-2982.

[24] Branco AC, Colaço R, Figueiredo-Pina CG, *et al*. Recent advances on 3D-printed zirconia-based dental materials: A review. *Materials* 2023, **16**: 1860.

[25] Bordia RK, Kang SJL, Olevsky EA. Current understanding and future research directions at the onset of the next century of sintering science and technology. *J Am Ceram Soc* 2017, **100**: 2314-2352.

[26] Drazin JW, Wollmershauser JA, Ryou H, *et al*. Pressureless low temperature sintering of nanocrystalline zirconia ceramics via dry powder processing. *J Am Ceram Soc* 2020, **103**: 60-69.

[27] von Steyern PV, Bruzell E, Vos L, *et al*. Sintering temperature accuracy and its effect on translucent yttria-stabilized zirconia: Flexural strength, crystal structure, tetragonality and light transmission. *Dent Mater* 2022, **38**: 1099-1107.

[28] Matsui K, Yoshida H, Ikuhara Y. Isothermal sintering effects on phase separation and grain growth in yttria-stabilized tetragonal zirconia polycrystal. *J Am Ceram Soc* 2009, **92**: 467-475.

[29] Lim CH, Alves LMM, Vardhaman S, *et al*. Two-step sintering suppresses grain growth and improves flexural strength of dental zirconia. *Dent Mater* 2025, **41**: 194-202.

[30] Zhang F, Inokoshi M, Batuk M, *et al*. Strength, toughness and aging stability of highly-translucent Y-TZP ceramics for dental restorations. *Dent Mater* 2016, **32**: e327-e337.

[31] Too TDC, Inokoshi M, Nozaki K, *et al*. Influence of sintering conditions on translucency, biaxial flexural strength, microstructure, and low-temperature degradation of highly translucent dental zirconia. *Dent Mater J* 2021, **40**: 1320-1328.

[32] Zhang XP, Wu X, Shi J. Additive manufacturing of zirconia ceramics: A state-of-the-art review. *J Mater Res Technol* 2020, **9**: 9029-9048.

[33] Wang XR, Tong WH, Shen YR, *et al*. Dynamic projection lithography for high-efficiency

Just Accepted

volumetric fabrication of thin-walled ceramics. *Addit Manuf* 2026, **116**: 105081.

[34] Zhang KQ, Meng QY, Qu ZL, *et al*. A review of defects in vat photopolymerization additive-manufactured ceramics: Characterization, control, and challenges. *J Eur Ceram Soc* 2024, **44**: 1361-1384.

[35] Guillon O, Gonzalez-Julian J, Dargatz B, *et al*. Field-assisted sintering technology/spark plasma sintering: Mechanisms, materials, and technology developments. *Adv Eng Mater* 2014, **16**: 830-849.

[36] Spusta T, Prajzler V, Maca K. Grain growth during capsule-free hot isostatic pressing. *Ceram Int* 2022, **48**: 25764-25771.

[37] Zhao RS, Yang HB, Liu XT, *et al*. Grain size refinement of additive manufactured Ce-TZP ceramics by coupled two-step pre-sintering and HIP. *J Adv Ceram* 2024, **13**: 621-629.

[38] Abbas S, Gal CW, Zhang S, *et al*. Flashing digital light processing based functionally graded additive manufacturing of zirconia dental crowns with simultaneous color and translucency gradation. *J Adv Ceram* 2025, **14**: 9221140.

[39] Scherrer SS, Cattani-Lorente M, Yoon S, *et al*. Post-hot isostatic pressing: A healing treatment for process related defects and laboratory grinding damage of dental zirconia? *Dent Mater* 2013, **29**: e180-e190.

[40] Feng B, Lugg NR, Kumamoto A, *et al*. Direct observation of oxygen vacancy distribution across yttria-stabilized zirconia grain boundaries. *ACS Nano* 2017, **11**: 11376-11382.

[41] Xiong Y, Luo L, Cheng Y, *et al*. Defects in the grain interiors of 3 mol% yttria-stabilized tetragonal zirconia polycrystal ceramics with 0.25 wt% alumina. *J Adv Ceram* 2024, **13**: 469-477.

[42] Zhao XH, Yan NP, Li YJ, *et al*. Dielectric barrier discharge-based defect engineering method to assist flash sintering. *J Adv Ceram* 2023, **12**: 1046-1057.

[43] Matsui K, Hosoi K, Feng B, *et al*. Ultrahigh toughness zirconia ceramics. *Proc Natl Acad Sci* 2023, **120**: e2304498120.

[44] McCusker LB, Von Dreele RB, Cox DE, *et al*. Rietveld refinement guidelines. *J Appl Crystallogr*

Just Accepted

1999, **32**: 36-50.

[45] Toby BH. R factors in Rietveld analysis: How good is good enough? *Powder Diffr* 2006, **21**: 67-70.

[46] Haremski P, Epple L, Wieler M, *et al*. A thermal grooving study of relative grain boundary energies of nickel in polycrystalline Ni and in a Ni/YSZ anode measured by atomic force microscopy. *Acta Mater* 2021, **214**: 116936.

[47] Shao R, Bonnell DA. Probing electrical transport across oxide interfaces by noncontact atomic force microscopy. *Appl Phys Lett* 2004, **85**: 4968-4970.

[48] Lankford J. Indentation microfracture in the Palmqvist crack regime: Implications for fracture toughness evaluation by the indentation method. *J Mater Sci Lett* 1982, **1**: 493-495.

[49] Anstis GR, Chantikul P, Lawn BR, *et al*. A critical evaluation of indentation techniques for measuring fracture toughness: I, direct crack measurements. *J Am Ceram Soc* 1981, **64**: 533-538.

[50] Andričević P, Johansen NF-J, Erives RI, *et al*. Does charge trapping affect subcritical crack growth behavior of yttria-stabilized zirconia? *J Am Ceram Soc* 2025, **108**: e20295.

[51] Harada K, Raigrodski AJ, Chung KH, *et al*. A comparative evaluation of the translucency of zirconias and lithium disilicate for monolithic restorations. *J Prosthet Dent* 2016, **116**: 257-263.

[52] Zhao RS, Liu XT, Li HZ, *et al*. Stronger and tougher nanosized dense ceria-doped tetragonal zirconia polycrystals by sinter-HIP. *J Eur Ceram Soc* 2023, **43**: 2282-2288.

[53] Krell A, Hutzler T, Klimke J. Transmission physics and consequences for materials selection, manufacturing, and applications. *J Eur Ceram Soc* 2009, **29**: 207-221.

[54] Raju K, Kim S, Yu JH, *et al*. Rietveld refinement and estimation of residual stress in GDC-LSCF oxygen transport membrane ceramic composites. *Ceram Int* 2018, **44**: 10293-10298.

[55] Syed K, Motley NB, Bowman WJ. Heterointerface and grain boundary energies, and their influence on microstructure in multiphase ceramics. *Acta Mater* 2022, **227**: 117685.

[56] Jiang L, Liao YM, Wan QB, *et al*. Effects of sintering temperature on the phase composition,

Just Accepted

microstructure and mechanical properties of zirconia ceramics. *J Mater Sci: Mater Med* 2011, **22**: 2429-2435.

[57] Fan JY, Yao S, Liu JL, *et al*. Effect of dynamic pressure on grain boundary energy and mechanical performance of high-strength zirconia ceramics fabricated via dynamic sinter forging. *J Eur Ceram Soc* 2026, **46**: 117898.

[58] Mullins WW. Theory of thermal grooving. *J Appl Phys* 1957, **28**: 333-339.

[59] Zhang W, Sachenko P, Schneibel JH. Kinetics of thermal grain boundary grooving for changing dihedral angles. *J Mater Res* 2002, **17**: 1495-1501.

[60] Matsui K, Ohmichi N, Ohgai M, *et al*. Grain boundary segregation-induced phase transformation in yttria-stabilized tetragonal zirconia polycrystal. *J Ceram Soc Jpn* 2006, **114**: 230-237.

[61] Serbena FC, Soares VO, Peitl O, *et al*. Internal residual stresses in sintered and commercial low expansion Li_2O-Al_2O_3-SiO_2 glass-ceramics. *J Am Ceram Soc* 2011, **94**: 1206-1214.

[62] Srinivasan R, De Angelis RJ, Ice G, *et al*. Identification of tetragonal and cubic structures of zirconia using synchrotron X-radiation source. *J Mater Res* 1991, **6**: 1287-1292.

[63] Witz G, Shklover V, Steurer W, *et al*. Phase evolution in yttria-stabilized zirconia thermal barrier coatings studied by Rietveld refinement of X-ray powder diffraction patterns. *J Am Ceram Soc* 2007, **90**: 2935-2940.

[64] Krogstad JA, Lepple M, Gao Y, *et al*. Effect of yttria content on the zirconia unit cell parameters. *J Am Ceram Soc* 2011, **94**: 4548-4555.

[65] Huang YL, Yang HB, Cheng SC, *et al*. On the sintering and grain growth of 1.5 mol% yttria-stabilized zirconia. *J Am Ceram Soc* 2025, **108**: e70140.

[66] Chen JQ, Wang WL, Sun XN, *et al*. Microstructure and mechanical properties of zirconia toughened nacre-like alumina ceramics. *Mater. Sci. Eng. A* 2022, **855**: 143908.

[67] Apetz R, van Bruggen MPB. Transparent alumina: A light-scattering model. *J Am Ceram Soc* 2003, **86**: 480-486.

Just Accepted

[68] Pecharromán C, Mata-Osoro G, Díaz LA, *et al*. On the transparency of nanostructured alumina: Rayleigh-Gans model for anisotropic spheres. *Opt Express* 2009, **17**: 6899-6912.

[69] Watanabe E, Yoshinari M. Changes in X-ray photoelectron spectra of yttria-tetragonal zirconia polycrystal brought about by Ar ion sputtering. *Appl Phys A* 2016, **122**: 339.

[70] Dashtbozorg B, Shi FZ, Tagliaferro A, *et al*. Plasma defect-engineering of bulk oxygen-deficient zirconia. *Acta Mater* 2024, **262**: 119457.

[71] Phani PS, Oliver WC. A critical assessment of the effect of indentation spacing on the measurement of hardness and modulus using instrumented indentation testing. *Mater Des* 2019, **164**: 107563.

Just Accepted